ANDERSON LOCALIZATION IN NON-HERMITIAN SYSTEMS: SKIN EFFECT AND SCALE-FREE LOCALIZATION

A THESIS SUBMITTED TO
THE GRADUATE SCHOOL OF ENGINEERING AND SCIENCE
OF BILKENT UNIVERSITY
IN PARTIAL FULFILLMENT OF THE REQUIREMENTS FOR
THE DEGREE OF
MASTER OF SCIENCE
IN
PHYSICS

By
Burcu Yılmaz
August 2024

Anderson Localization in non-Hermitian Systems: Skin Effect and Scale-Free Localization
By Burcu Yılmaz
August 2024

We certify that we have read this thesis and that in our opinion it is fully adequate, in scope and in quality, as a thesis for the degree of Master of Science.

Ceyhun Bulutay(Advisor)

Cem Yüce(Co-Advisor)

Hâldun Sevinçli

Seymur Jahangirov

Approved for the Graduate School of Engineering and Science:

Orhan Arıkan
Director of the Graduate School

ABSTRACT

ANDERSON LOCALIZATION IN NON-HERMITIAN SYSTEMS: SKIN EFFECT AND SCALE-FREE LOCALIZATION

Burcu Yılmaz
M.S. in Physics
Advisor: Ceyhun Bulutay
Co-Advisor: Cem Yüce
August 2024

Localization properties of eigenstates change according to the lattice model. A Hatano-Nelson model with asymmetric hopping constants exhibit non-Hermitian skin effect(NHSE) where eigenstates localize near the edge of the lattice, the localization length is finite and does not depend on the system size. With introducing disorder to the Hatano-Nelson model, skin states start to become Anderson localized states. At a critical disorder strength all skin states become Anderson localized states. Since localization length of skin states does not depend on the system size, this model exhibits a size-independent Anderson localization. When the Hatano-Nelson model is modified as a 1D Hermitian lattice with an impurity, new model exhibits scale-free localized (SFL) states where unlike skin states, localization length scales with the system size. SFL states have a spatial profile that does not change as the system size varies. With the introduction of disorder into the system with SFL states, the interplay between SFL and Anderson localized states is observed. At the critical disorder strength, all states become Anderson localized states. Since localization length of SFL states scales with system size, a size-dependent Anderson transition occurs.

Keywords: Hatano-Nelson model, non-Hermitian skin effect, scale-free localization, critical disorder strength, Anderson localization, PT-symmetry, inverse participation ratio.

ÖZET

HERMİTYEN OLMAYAN SİSTEMLERDE ANDERSON YERELLEŞMESİ: DERİ ETKİSİ VE ÖLÇEKTEN BAĞIMSIZ YERELLEŞME

Burcu Yılmaz
Fizik, Yüksek Lisans
Tez Danışmanı: Ceyhun Bulutay
İkinci Tez Danışmanı: Cem Yüce
Ağustos 2024

Özvektörlerin yerelleşme özellikleri örgü modeline bağlı olarak değişir. Asimetrik bağlantı terimlerine sahip bir Hatano-Nelson modeli, özvektörlerin örgünün sınırında yerelleştiği Hermityen olmayan deri etkisi gösterir. Burada yerelleşme uzunluğu sonludur ve sistem büyüklüğüne bağlı değildir. Hatano-Nelson modeline düzensizlik eklediğimizde, deri etkisi özvektörleri Anderson yerelleşen özvektörlere dönüşmeye başlar. Kritik bir düzensizlik şiddetinde, tüm deri etkisi özvektörleri Anderson yerelleşen özvektörlere dönüşür. Deri etkisi özvektörlerinin yerelleşme uzunluğu, sistem büyüklüğüne bağlı olmadığı için, bu model, büyüklükten bağımsız bir Anderson yerelleşmesi sergilemektedir. Hatano-Nelson modeli, bir boyutlu içinde safsızlık bulunan bir Hermityen örgü olarak değiştirildiğinde, yeni model, deri etkisi özvektörleri aksine, yerelleşme uzunluğunun sistem büyüklüğüne bağlı olduğu ölçekten bağımsız yerelleşme özvektörler sergiler. Ölçekten bağımsız yerelleşme durumların sistem büyüklüğü değiştikçe değişmeyen bir uzaysal profili vardır. Ölçekten bağımsız yerelleşme durumlarına sahip sisteme düzensizlik eklendiğinde, ölçekten bağımsız ve Anderson yerelleşme durumları arasındaki etkileşim gözlemlenir. Kritik düzensizlik şiddetinde, tüm durumlar Anderson yerelleşme durumlarına dönüşür. Ölçekten bağımsız durumlarının yerelleşme uzunluğu sistem büyüklüğüyle ölçeklendiğinden, büyüklüğe bağlı bir Anderson geçişi gerçekleşir.

Anahtar sözcükler: Hatano-Nelson modeli, Hermityen olmayan deri etkisi, ölçekten bağımsız yerelleşme, kritik düzensizlik gücü, Anderson yerelleşmesi, PT-simetri, ters katılım oranı.

Acknowledgement

I would like to express my deepest gratitude to my advisors, professors, Ceyhun Bulutay and Cem Yüce, for their guidance and continuous support throughout my academic journey. Their optimism and expertise have greatly influenced my research, I have learned so much from them and I am truly fortunate to have had the opportunity to work under their supervision.

I would also like to extend my sincere thanks to professors, Hâldun Sevinçli and Seymur Jahangirov for their time in reading and reviewing my work. Their valuable comments significantly improved my thesis.

The numerical simulations reported in this thesis were partially performed at Türkiye Bilimsel ve Teknolojik Araştırma Kurumu (TUBİTAK) ULAKBİM, High Performance, and Grid Computing Center (TRUBA resources).

I would like to thank my family, my mother Deniz, my father Mehmet, my brother Emre, and our cat Şeker for their continuous love and support. They have always been there for me, supporting me under all circumstances, and encouraging me throughout my life.

Lastly, I would like to extend my heartfelt thanks to the people who have been a crucial part of my life: Ahmet Çalışkan, Efe Yelesti, Ezgi Danacı, Sena Nalbant, Silvana Abi Mershed, Yankı Suveren, and Yılmaz Can Yüksek. They fill my life with joy and unforgettable memories, and I feel incredibly lucky to have them by my side.

Contents

1 Introduction **1**

1.1 Basic Concepts 2

1.1.1 Parity-Time Symmetry 2

1.1.2 Anderson Localization 3

1.1.3 Non-Hermitian Skin Effect 4

1.1.4 Scale-free Localization 4

1.1.5 Localization Length and Inverse Participation Ratio 5

1.2 Outline of This Thesis 6

2 Non-Hermitian Skin Effect and Spectral Topology **7**

2.1 Non-Bloch Band Theory 7

2.2 Bulk-Boundary Correspondence 9

2.3 Non-Hermitian Skin Effect 10

2.4 Hatano-Nelson Model 10

2.5 Winding number 20

3 Scale-free Localization 22

3.1 Energy Spectrum under GBC 26

3.2 Results and IPR values 30

4 Anderson Localization in non-Hermitian Systems: The Hatano-Nelson Model 34

4.1 Introducing Disorder 34

4.2 Competition Between NHSE and Anderson Localization 36

5 1D Hermitian Lattice with a non-Hermitian Impurity and Scale Free Localization 42

5.1 The Model 43

5.2 Distinct Parameter Regions 45

5.3 Results 47

6 Size-Dependent Anderson Localization 53

6.1 Extended Model 53

6.2 Results 56

6.2.1 General Traits 56

6.2.2 Critical Disorder Strength 57

6.2.3 PT-unbroken and PT-restoration Regions 59

6.2.4 PT-broken Region 59

6.2.5 IPR Values 61

7 Conclusion **66**

List of Figures

1.1 Two coupled subsystems with gain and loss. g is the coupling strength. 3

1.2 The outline of this thesis as a mind map. Anderson Localization (AL), non-Hermitian skin effect (NHSE), scale-free localization (SFL), Hatano-Nelson model (HN). 6

2.1 1D non-Hermitian tight-binding Hatano-Nelson model with asymmetric hoppings, $J_R^* \neq J_L$. 10

2.2 Eigenvalues and eigenvectors for the disorder-free HN-model under PBC and OBC when $J_R = 0.5$, $J_L = 1$ and $N = 40$. (a) Eigenvalues under PBC, shown in red dots, form a ellipse on the complex plane with major, minor radii being $|J_R \pm J_L|$. Eigenvalues under OBC, shown in blue crosses, lie on the real axis in the interval of $[-2\sqrt{J_R J_L}, 2\sqrt{J_R J_L}]$. (b) Eigenstates under PBC, shown in red, and OBC, shown in blue, for the disorder-free HN-model. NHSE can be seen in OBC states where the eigenstates are localized at the left edge. (c) Energy spectrum under PBC vs wave vector k. . 16

2.3 Eigenvalues and eigenvectors for the disorder-free HN-model under PBC and OBC when $J_R = 1$, $J_L = 0.5$ and $N = 40$. (a) Eigenvalues under PBC, shown in red dots, form a ellipse on the complex plane with major, minor radii being $|J_R \pm J_L|$. Eigenvalues under OBC, shown in blue crosses, lie on the real axis in the interval of $[-2\sqrt{J_R J_L}, 2\sqrt{J_R J_L}]$. (b) Eigenstates under PBC, shown in red, and OBC, shown in blue, for the disorder-free HN-model. NHSE can be seen in OBC states where the eigenstates are localized at the right edge. (c) Energy spectrum under PBC vs wave vector k. 17

2.4 Eigenvalues and eigenvectors for the disorder-free HN-model under PBC and OBC when $J_R = 1$, $J_L = 0$ and $N = 40$. (a) Eigenvalues under PBC form a ellipse on the complex plane while eigenvalues under OBC, coalesce into each other. (b) Eigenstates under PBC, shown in red, and OBC, shown in blue, for the disorder-free HN-model. NHSE can be seen in OBC states where the eigenstates are localized at the right edge, coalescing into each other. (c) Energy spectrum under PBC vs wave vector k. 18

2.5 Eigenvalues and eigenvectors for the disorder-free HN-model under PBC and OBC when $J_R = 0$, $J_L = 1$ and $N = 40$. (a) Eigenvalues under PBC form a ellipse on the complex plane while eigenvalues under OBC, coalesce into each other. (b) Eigenstates under PBC, shown in red, and OBC, shown in blue, for the disorder-free HN-model. NHSE can be seen in OBC states where the eigenstates are localized at the left edge, coalescing into each other. (c) Energy spectrum under PBC vs wave vector k. 19

2.6 (a) For $|J_R| < |J_L|$, energy spectrum winds around the origin in counterclockwise direction indicating $w = 1$ and for $|J_R| > |J_L|$, energy spectrum winds around the origin in clockwise direction indicating $w = -1$, (b) $w = 0$. 21

3.1 1D non-Hermitian tight-binding Hatano-Nelson model with asymmetric hoppings, $J_R^* \neq J_L$ with Generalized Boundary Conditions. 23

3.2 IPR values are plotted as a function of ζ_R and ζ_L for (a) $N = 10$, (b) $N = 20$, (c) $N = 40$ and (d) $N = 80$. Common parameters are $J_R = 1$ and $J_L = 0.85$. When lattice size is increasing, there is a corresponding decrease in the IPR value. 31

3.3 PBC, OBC and GBC cases are shown in red, blue and lime respectively. (a) eigenvalues of $a1$, (b) eigenvectors of $a1$. 32

3.4 PBC, OBC and GBC cases are shown in red, blue and lime respectively. (a) eigenvalues of $a2$, (b) eigenvectors of $a2$. 32

3.5 PBC, OBC and GBC cases are shown in red, blue and lime respectively. (a) eigenvalues of $a3$, (b) eigenvectors of $a3$. 33

3.6 PBC, OBC and GBC cases are shown in red, blue and lime respectively. (a) eigenvalues of $a4$, (b) eigenvectors of $a4$. 33

4.1 Introducing random on-site potentials to 1D non-Hermitian tight-binding Hatano-Nelson model with asymmetric hoppings, $J_R^* \neq J_L$. 35

4.2 Eigenstates under OBC for $J_R = 0.5$, $J_L = 1$, $N = 40$ and different disorder strengths: (a) $W = 0$, NHSE; (b) $W = 2$, coexistence of NHSE and Anderson localization; (c) $W = 4$, coexistence of NHSE and Anderson localization; (d) $W = 6$, Anderson localization. . . . 38

4.3 Eigenvalues corresponding to Fig. 4.2 under OBC (blue) and PBC (red) for $J_R = 0.5$, $J_L = 1$, $N = 40$, and various disorder strengths: (a) $W = 0$, the PBC spectrum forms a loop in the complex energy plane while OBC loops lie on the real axis; (b) $W = 2$, the PBC loop begins to deform; (c) $W = 4$, the PBC loop continues deforming; (d) $W = 6$, both the PBC and OBC spectra lie on the real axis, and the corresponding states are Anderson localized. . . 39

4.4 Eigenvalues under PBC for $N = 1000$ and different disorder strenghts. 40

5.1 1D Hermitian lattice with a non-Hermitian impurity. t's are the Hermitian hoppings between the neighboring sites and non-Hermitian impurity at site m has $\delta - \gamma$ to the right and $\delta + \gamma$ to the left. 43

5.2 Phase diagram of the 1D lattice described by Eq. 5.1 for the disorder-free case. The lattice size is $N = 40$, $t = 1$, and the impurity is positioned at $m = 20$. The color map represents the number of complex eigenvalues. The cyan line, where $\gamma = \sqrt{\delta^2 - t^2}$, indicates the transition to SFL states for all states. The black dashed lines, given by $\gamma = |\delta - t|$ and $\gamma = \delta + t$, represent the phase boundaries of PT-symmetry for there regions: PT-unbroken region where $\gamma < |\delta - t|$, PT-broken region where $|\delta - t| < \gamma < \delta + t$, PT-restoration region where $\gamma > \delta + t$. Points a to e lie along the vertical axis where $\delta = 5t$. 46

5.3 (a1) Eigenvalues and (a2) Eigenvectors of the PT-unbroken region. Eigenvalues and eigenvectors are categorized as follows: extended bulk states with real eigenvalues (magenta) and two impurity-bound states with real eigenvalues (blue). 48

5.4 (b1) Eigenvalues and (b2) Eigenvectors of the PT-broken region. Eigenvalues and eigenvectors are categorized as follows: extended states with real eigenvalues (magenta), two impurity-bound states with real eigenvalues (blue) and SFL states forming a loop on the complex plane (lime). 48

5.5 (c1) Eigenvalues and (c2) Eigenvectors of the PT-broken region. Eigenvalues and eigenvectors are categorized as follows: SFL states form a loop on the complex plane (lime). 49

5.6 (d1) Eigenvalues and (d2) Eigenvectors of the PT-broken region. Eigenvalues and eigenvectors are categorized as follows: extended states with real eigenvalues (magenta), two impurity-bound states with complex eigenvalues (blue) and SFL states with real and complex eigenvalues (lime). 50

5.7 (e1) Eigenvalues and (e2) Eigenvectors of the PT-restoration region. Extended states with real eigenvalues and two impurity-bound states with complex eigenvalues. 50

5.8 Eigenstates when $\gamma = \sqrt{\delta^2 - t^2}$ for lattice sizes (a) $N = 40$ and (b) $N = 1000$. Impurity is positioned at $m = N/2$. 51

5.9 Energy spectrum of the disorder free case with respect to γ for a fixed $\delta = 5t$ value. Real parts of the eigenvalues are marked in red, imaginary parts of the eigenvalues are marked in blue. 52

6.1 1D Hermitian lattice with a non-Hermitian impurity. t's are the Hermitian hoppings between the neighboring sites, on-site potentials are V_m and non-Hermitian impurity at site m has $\delta - \gamma$ to the right and $\delta + \gamma$ to the left. The Hermitian Anderson model shows an Anderson transition at any non-zero disorder strength. Adding a single impurity makes the Anderson transition point dependent on the system size. In the Hermitian Anderson model, extended states become Anderson localized states at the Anderson transition point. However, when a single impurity is introduced, both extended and SFL states turn into Anderson localized states at the transition point. This leads to a significant shift and size dependency in the Anderson transition point. 54

6.2 Phase diagram of the 1D lattice in Eq.6.1 for different W, disorder strength values. The number of complex eigenvalues are coded in the color bar as a function of δ and γ for $N = 40$ and (a) $W = 0$, "Disorder-free" , (b) $W = 1$, (c) $W = 2$, (d) $W = 3$, (e) $W = 4$, (f) $W = 5$ 57

6.3 Phase diagram of the critical disorder strength (W_c) as a function of δ and γ for different system sizes: (a) $N = 40$, (b) $N = 80$, (c) $N = 160$, (d) $N = 1000$ for $t = 1$. White dashed lines are given by $\gamma = |\delta - t|$ and $\gamma = \delta + t$ and represent the phase boundaries of the PT-symmetry for there regions. PT-unbroken region where $\gamma < |\delta - t|$, PT-broken region where $|\delta - t| < \gamma < \delta + t$, PT-restoration region where $\gamma > \delta + t$. Results are averaged over many random potential realizations. Impurity is positioned at $m = N/2$. Competition between Anderson and SFL states. Anderson and SFL states coexist until $W = W_c$ in which Anderson transition occurs. 58

6.4 Ratio of the Anderson localized states over all states at $\gamma = \sqrt{\delta^2 - t^2}$. 60

6.5 The minimum IPR among all IPR values as a function of disorder strength, averaged over 10000 realizations for both Hermitian (yellow) and non-Hermitian (lime for $W < W_c$ and green for $W \geq W_c$) cases when $\gamma = \sqrt{\delta^2 - t^2}$ for (a) $N = 40$, (b) $N = 80$ (c) $N = 160$. 63

6.6 Average IPR values at $W = W_c$ for various system sizes: (a) $N = 40$, (b) $N = 80$, (c) $N = 160$, and (d) $N = 1000$. The white dashed lines are given by $\gamma = |\delta - t|$ and $\gamma = \delta + t$. Notice the difference in average IPR values between the PT-broken region and the other two regions at the same disorder strength. This difference arises because SFL states transform into Anderson localized states in the PT-broken region, whereas extended states undergo this transformation in the other regions. Impurity is positioned at $m = N/2$. 65

List of Tables

4.1 Relationship between critical disorder strength W_c and lattice size N in the Hatano-Nelson model. The results show no size dependency. 41

Chapter 1

Introduction

Physical systems can be classified as being open or closed depending on the boundary conditions. Closed systems, being isolated from their environments, do not interact with the external surroundings and they are represented by a Hermitian Hamiltonian, ($\hat{H} = \hat{H}^{\dagger}$) [1, 2, 3, 4, 5]. When a system is Hermitian, its eigenvalues guaranteed to be real and its eigenvectors are orthogonal to each other. Quantities like energy, particle number (probability in the context of quantum mechanics) are conserved in Hermitian systems. Closed systems are useful as idealized systems, but they cannot be observed in a laboratory environment, as performing the necessary measurements causes the system to interact with its surroundings, effectively making it an open system. Open systems are not isolated from their environment and interact with external surroundings. Open systems reflect the physical reality and in nature, particle number and energy are not conserved due to flow of energy, information, or similar kinds of excitations [6]. When Hermiticity is broken, system needs a non-Hermitian formalism, ($\hat{H} \neq \hat{H}^{\dagger}$). Non-Hermitian models describe the behaviour of the open systems and in addition reveal new phenomena that is coming from the non-Hermiticity including open quantum systems, electronic systems with interactions, and classical systems with gain or loss [7].

1.1 Basic Concepts

In Hermitian systems, bulk states are generally insensitive to local impurities except for a few impurity-induced bound states [8]. However, when a local non-Hermitian impurity is introduced, it causes significant changes in the system's spectral properties [9, 10, 11, 12, 13, 14]. Specifically, the breaking of Parity-Time (PT) symmetry can lead to changes in the energy spectrum, resulting in imaginary parts of the eigenvalues accompanied by topological transitions [15, 16, 17, 18, 19, 20]. Recent studies have explored several aspects of non-Hermitian systems such as the non-Hermitian skin effect (NHSE) [21, 22], and scale-free localization (SFL) [23, 24].

Now, we will give some basic information about the key concepts this thesis uses.

1.1.1 Parity-Time Symmetry

Hermiticity ensures the real eigenvalues, however non-Hermitian systems can also have real eigenvalues if the so called parity-time (PT) symmetry is satisfied [2, 4, 25, 26, 27, 5, 28, 29]. Here, $\hat{P}$ represent the parity operator which changes the sign of spatial coordinates ($\vec{r} \rightarrow -\vec{r}$) and $\hat{T}$ represents the time reversal operator which reverses the direction of time ($t \rightarrow -t$). PT-symmetric Hamiltonian commutes with the product parity and the time reversal operators,

$$\hat{P}\hat{T}\hat{H}(\hat{P}\hat{T})^{-1} = \hat{H}. \tag{1.1}$$

Two non-isolated subsystems can be coupled with its time-reversed version like in Fig. 1.1 to conserve the probability. The original subsystem $H_{original}$ and the time-reversed subsystem $H_{time-reversed}$ has opposite flux of probability which cancel out each other. Thus, the operator (i.e., matrix) $H_{coupled}$ in Eq. 1.3 has no net flux of probability.

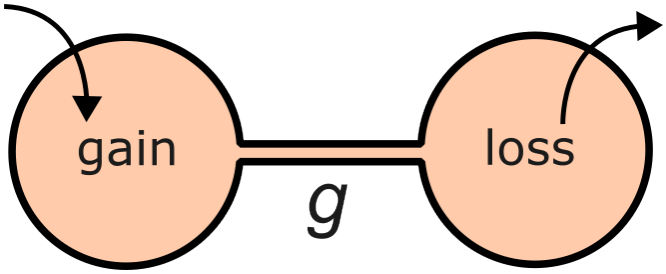

Figure 1.1: Two coupled subsystems with gain and loss. g is the coupling strength.

$$\begin{aligned} \hat{H}_{original} &:= [a + ib], \\ \hat{H}_{time-reversed} &:= \hat{T}\hat{H}\hat{T^{-1}} := [a - ib], \end{aligned} \tag{1.2}$$

$$H_{coupled} = \begin{bmatrix} a + ib & g \\ g & a - ib \end{bmatrix}, \tag{1.3}$$

where g is the coupling constant. Eigenvalues of $H_{coupled}$ can be written as $E_{\pm} = a \pm \sqrt{g^2 - b^2}$.

When $g^2 < b^2$, subsystems are weakly coupled. Eigenvalues are complex, implying that PT-symmetry is broken. One subsystem will grow (gain) and other will decay (loss) with time, thus the overall system is not in an equilibrium. When $g^2 > b^2$, subsystems are strongly coupled that now system is in equilibrium. Note that even though $H_{coupled}$ is not Hermitian, it has real eigenvalues. PT-symmetry is unbroken [1, 30].

1.1.2 Anderson Localization

Random potentials introduced throughout a lattice cause impurities or irregularities. In 1958, Anderson stated that when materials are disordered, waves change their behaviours accordingly to these impurities. As a result, waves are unable to move freely through the material and become localized around the impurities. This phenomena is known as the Anderson Localization [31]. Here, a critical energy which sets the so-called *mobility edge* plays a crucial role on separating localized states from extended states. Mobility edge is an energy threshold;

localized states are the ones with energies below the threshold and delocalized states are the ones with energies that are higher than the mobility edge threshold [32, 33, 34, 35, 36, 37, 38].

1.1.3 Non-Hermitian Skin Effect

Non-Hermitian skin effect (NHSE) is caused from the non-Hermiticity of the system and characterized by the extreme sensitivity of the spectrum to the boundary conditions [39, 40, 41]. This high sensitivity to boundaries leads to the localization of the eigenstates at the edges and mobility edge in Anderson localization [32, 33, 34, 35, 36, 37, 22, 42, 43, 44]. Since NHSE is sensitive to the boundary condition, it is important to observe whether it can survive when boundary condition is changing from open boundary conditions (OBC) to periodic boundary conditions (PBC).

Recently, NHSE gave rise to the generalization of Brillouin zone under the OBC in both Hermitian and non-Hermitian systems [45]. Lately, NHSE has also been studied as induced by on-site dissipations [46], under generalized boundary conditions [38, 47]. Experimental demonstrations of the NHSE such as in electrical circuits [48, 49, 50] and in acoustic setups are studied [48, 49, 50].

1.1.4 Scale-free Localization

When an impurity with non-Hermitian coupling is introduced to a Hermitian lattice, it breaks the periodicity of the lattice and gives rise to the scale-free localized (SFL) states where localization length scales with the system size [51, 8, 52]. [9, 10, 11, 13, 14] The scaling rule of the SFL length is shown to be determined by the geometry of the generalized Brillouin zone [53]. States become localized near this impurity. Scale-free localization is the type of localization where it is induced by the non-Hermiticity of the system unlike Anderson localization where localization is due to the disorder in the lattice. Thus, PT-symmetry breaking is

often associated with scale-free localization [54]. SFL has recently been expanded to many-body interactions [54], and it is experimentally observed in electric circuit lattices having a non-Hermitian defect [55].

1.1.5 Localization Length and Inverse Participation Ratio

The extent to which a wave function is spread out or localized in a system refers to the localization length. It indicates the distance over which the wave function remains significant before it begins to decrease sharply. It is the distance that the wave function effectively extends [56].

For skin states and Anderson localized states, localization length is not dependent on the system size. Localization length is finite and it is determined by the disorder of the system. For example, when system size increases, localization length of skin states and Anderson localized states stays the same. For scale-free localization, localization length is proportional to the system size. If the system size is increased, localization length of the SFL states increases accordingly. When system size is increased the distance will be increased too [57, 51, 8, 52].

Inverse participation ratio (IPR) is a quantitative metric as to how localized or delocalized given eigenstates are in a system [58]. If the wave function at a lattice site, n is ψ_n, it is obtained using,

$$\mathrm{IPR} = \frac{\sum_n |\psi_n|^4}{\left(\sum_n |\psi_n|^2\right)^2}. \tag{1.4}$$

IPR ranges between 0 and 1: completely localized states have 1 and it is close to 0 for delocalized states which extends and spreads throughout the lattice.

1.2 Outline of This Thesis

In this thesis, we first analyze the topological properties of the 1D Hatano-Nelson model, which exhibits the NHSE in the absence of disorder in Chapter 2. Using the Hatano-Nelson model under generalized boundary conditions (GBC), we observe scale-free localization in Chapter 3. Then, in Chapter 4, we introduce random on-site energies into the Hatano-Nelson model and examine the competition between NHSE and Anderson localization. We determine the critical disorder strength W_c, which is the disorder strength where all states become Anderson localized. Here, we will demonstrate the size-independent Anderson localization. In Chapter 5, we restore the disorder-free lattice to a Hermitian form but introduce an impurity non-reciprocally coupled to give rise to SFL states. In Chapter 6, we introduce disorder into the lattice and observe the competition between SFL and Anderson localized states. Here, we illustrate the emergence of size-dependent Anderson localization. Fig. 1.2 presents the outline of this thesis in the form of a mind map.

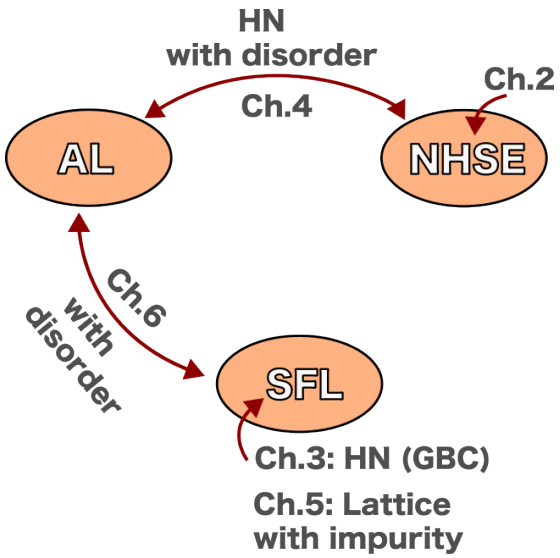

Figure 1.2: The outline of this thesis as a mind map. Anderson Localization (AL), non-Hermitian skin effect (NHSE), scale-free localization (SFL), Hatano-Nelson model (HN).

Chapter 2

Non-Hermitian Skin Effect and Spectral Topology

In this chapter, we analyze and provide a discussion about the topology of non-Hermitian systems, the bulk-boundary correspondence and the behaviours of the eigenvalues and eigenstates of Hatano-Nelson model and thus the non-Hermitian skin effect (NHSE).

2.1 Non-Bloch Band Theory

In Hermitian systems, the difference of the energy spectra under PBC and OBC decreases with increasing lattice size. As the lattice size increases, the effect of boundary conditions become insignificant. For large lattice sizes, the energy bands of PBC are asymptotically same as the energy levels of OBC. Bloch band theory is used to state the electronic structure with using the Bloch wave number k [59]. Bloch wave number is real for Hermitian systems. For non-Hermitian systems, Bloch band theory fails to describe the bulk and boundary properties because of the requirement of a complex wave number $k \in \mathbb{C}$. Defining $\beta = e^{ik}$, β lies on a complex loop and does not necessarily represent a unit circle [60, 61].

Non-Bloch theory is used to describe the structure of non-Hermitian systems using the complex k, energy bands of the system align with the energy levels of the system [60].

Let us first consider a 1D tight-binding lattice under OBC. Hamiltonian of the lattice is given as

$$\hat{H} = \sum_{n} \sum_{i=-L}^{L} \sum_{\mu,\nu=1}^{q} J_{i,\mu\nu} \hat{c}^{\dagger}_{n+i,\mu} \hat{c}_{n,\nu}, \tag{2.1}$$

where $\hat{c}_{n,\mu}$ ($\hat{c}^{\dagger}_{n,\mu}$) annihilation (creation) operators with $\mu = 1, \ldots, q$ at n-th unit cell, L is the hopping range, q represents independent degrees of freedom (sublattices, spins, or orbitals) and $J_{i,\mu\nu}$ represents the hopping constant to the left and right to ith neighboring unit cell. If the Hamiltonian is non-Hermitian, the hopping constants satisfy $J_{i,\mu\nu} \neq J^{*}_{-i,\mu\nu}$. The eigenvalue equation is given by the Schrödinger equation is $\hat{H} |\psi\rangle = E |\psi\rangle$, where $|\psi\rangle$ can be written as

$$|\psi\rangle = \begin{pmatrix} \vdots \\ \psi_{1,q} \\ \psi_{2,1} \\ \vdots \end{pmatrix}, \tag{2.2}$$

and ψ's can be written as a linear combination of

$$\psi_{n,\mu} = \sum_{j} \phi^{(j)}_{n,\mu}, \tag{2.3}$$

where $\phi^{(j)}_{n,\mu} = (\beta_j)^n \phi^{(j)}_{\mu}$ with $\mu = 1, \ldots, q$ [60].

For $\beta = \beta_j$

$$\sum_{\nu=1}^{q} \mathcal{H}(\beta)_{\mu\nu} \phi_{\nu} = E\phi_{\mu}, \quad (\mu = 1, \cdots, q), \tag{2.4}$$

where $\nu = 1, \ldots, q$ and generalized Bloch Hamiltonian can be written as

$$\mathcal{H}(\beta)_{\mu\nu} = \sum_{i=-L}^{L} J_{i,\mu\nu} \beta^{i}, \tag{2.5}$$

where $\mu, \nu = 1, \ldots, q$.

For a Hermitian case, Eq. 2.4 gives the Bloch eigenstates. The eigenvalue equation for the Hamiltonian $H(\beta)$ can be written as

$$\det[\mathcal{H}(\beta) - E] = 0. \tag{2.6}$$

Now, we want to determine the generalized Brillouin zone, C_β. It determines the continuum bands. When $j = 1, \ldots, 2M$, for β_j satisfies

$$|\beta_1| \leq |\beta_2| \leq \cdots \leq |\beta_{2M-1}| \leq |\beta_{2M}|. \tag{2.7}$$

In order to get continuum bands, β must satisfy

$$|\beta_M| = |\beta_{M+1}|, \tag{2.8}$$

and the trajectory of Eq. 2.8 determines the generalized Brillouin zone, C_β. For a Hermitian system, C_β is a unit circle where $|\beta_M| = |\beta_{M+1}| = 1$ [60].

2.2 Bulk-Boundary Correspondence

Bulk-boundary correspondence provides the relation between the topological bulk properties and the edge states in Hermitian systems [62]. In a topological phase, topological invariants remains constant when the system's parameters are deformed. Bulk topological invariants determines the presence of boundary states and defined using the Bloch Hamiltonian [63]. We will observe how bulk-boundary correspondence is being obscured and modified in non-Hermitian systems which is related to the emergence of the NHSE [63, 12]. NHSE causes bulk modes to localize on the boundaries of the lattice thus breaking the bulk-boundary correspondence [39, 64].

2.3 Non-Hermitian Skin Effect

Non-Hermitian systems often show a phenomenon called NHSE in which a significant number of eigenstates are localized at the edge of the lattice [21]. NHSE which is driven by the non-Hermiticity of the system, arises due to asymmetric hopping in the lattice and demonstrates high sensitivity to boundaries meaning that presence and position of the boundaries change the behaviour of the eigenstates. For example, we cannot observe the NHSE under PBC because there are no edges for the eigenstates to localize. High sensitivity to boundaries which leads to the edge localization of eigenstates, motivated the generalization of Brillouin zone under the open boundary conditions in both Hermitian and non-Hermitian systems [45].

2.4 Hatano-Nelson Model

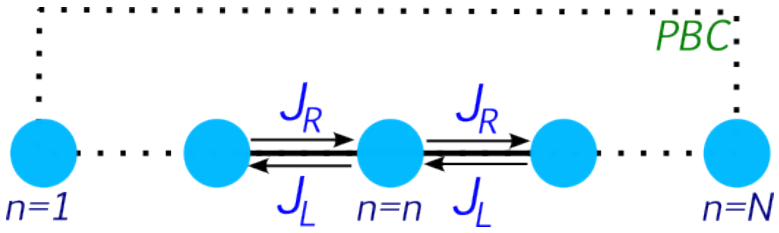

Figure 2.1: 1D non-Hermitian tight-binding Hatano-Nelson model with asymmetric hoppings, $J_R^* \neq J_L$.

In order to analyze and understand the non-Hermitian topological properties, we start with the Hatano-Nelson model. It is a 1D non-Hermitian tight-binding lattice model with asymmetric hoppings [65, 66, 67]. The Hamiltonian of the model as illustrated in Fig. 2.1 can be expressed as

$$\hat{H} = \sum_{n=1}^{N} (J_R \hat{c}_{n+1}^{\dagger} \hat{c}_n + J_L \hat{c}_n^{\dagger} \hat{c}_{n+1}), \tag{2.9}$$

where $\hat{c}_n$ ($\hat{c}_n^\dagger$) annihilation (creation) operators at site n, J_R is the hopping constant to the right, J_L is the hopping constant to the left with $J_R^* \neq J_L$, and N is the lattice size. To impose PBC, we assume that $n = 1$ coincides with $n = N + 1$ ($\hat{c}_1 = \hat{c}_{N+1}$).

Matrix representation of the single-particle Hamiltonian in Eq. 2.9 is

$$\begin{pmatrix} 0 & J_L & 0 & \cdots & 0 & 0 & \cdots & 0 & J_R \\ J_R & 0 & J_L & \cdots & 0 & 0 & \cdots & 0 & 0 \\ 0 & J_R & 0 & J_L & 0 & 0 & \cdots & 0 & 0 \\ 0 & 0 & J_R & \ddots & \vdots & \vdots & & \vdots & \vdots \\ \vdots & \vdots & \vdots & & \vdots & & \ddots & \vdots & \vdots \\ 0 & 0 & 0 & \cdots & 0 & 0 & \cdots & 0 & J_L \\ J_L & 0 & 0 & \cdots & 0 & 0 & \cdots & J_R & 0 \end{pmatrix}_{N\times N} \tag{2.10}$$

The elements J_R and J_L that are highlighted in red to indicate that they appear under PBC and disappear under OBC.

We will let $J_R, J_L \in \mathbb{R}$, assume PBC and write down the Hamiltonian in momentum space using Fourier transformations [32]

$$\hat{c}_n = \frac{1}{\sqrt{N}} \sum_k e^{ikn} \hat{c}_k, \qquad \hat{c}_n^\dagger = \frac{1}{\sqrt{N}} \sum_{k'} e^{-ik'n} \hat{c}_{k'}^\dagger, \tag{2.11}$$

where $k = \frac{2\pi m}{N}$ and $m = 0, 1, ..., N - 1$.

Canonical commutation relation states that

$$[\hat{c}_n, \hat{c}_n^\dagger] = \delta_{n,n'} \hat{\mathbb{1}} \tag{2.12}$$

$$
\begin{aligned}
[\hat{c}_n, \hat{c}_n^\dagger]_\mp = & \\
&= \hat{c}_n \hat{c}_n^\dagger \mp \hat{c}_n^\dagger \hat{c}_n \\
&= \frac{1}{N} \sum_{n,k,k'} e^{i(k-k')n} \hat{c}_k \hat{c}_{k'}^\dagger \mp \frac{1}{N} \sum_{n,k,k'} e^{i(k-k')n} \hat{c}_{k'}^\dagger \hat{c}_k \\
&= \frac{1}{N} \sum_{n,k,k'} e^{i(k-k')n} [\hat{c}_k, \hat{c}_{k'}^\dagger]_\mp
\end{aligned}
\tag{2.13}
$$

CCR satisfies if $[\hat{c}_k, \hat{c}_{k'}^\dagger] = \delta_{k,k'} \hat{\mathbb{1}}$.

Let $k = k'$

$$
[\hat{c}_n, \hat{c}_n^\dagger] = \frac{1}{N} \sum_{n,k} e^{i(k-k)n} [\hat{c}_k, \hat{c}_k^\dagger]_\mp = \hat{\mathbb{1}} \tag{2.14}
$$

Now, let us express Eq. 2.9 in terms of $\hat{c}_k$, $\hat{c}_k^\dagger$ operators by using Eq. 2.11-2.14

$$
\hat{H} = \frac{1}{N} \sum_{n,k,k'} e^{i(k-k')n} \hat{c}_{k'}^\dagger \hat{c}_k (J_R e^{-ik'} + J_L e^{ik}). \tag{2.15}
$$

Using the identity $\frac{1}{N} \sum_{n=1}^{N} e^{i(k-k')n} = \delta_{k,k'}$ and let $k = k'$

$$
\begin{aligned}
\hat{H} &= \sum_k \hat{c}_k^\dagger \hat{c}_k (J_R e^{-ik} + J_L e^{ik}) \\
&= \sum_k \hat{n}_k E_k,
\end{aligned}
\tag{2.16}
$$

where $\hat{n}_k$ is the number operator and where

$$
E_k = (J_R + J_L) \cos k + i(J_L - J_R) \sin k. \tag{2.17}
$$

Eq. 2.17 shows the energy spectrum of the Hamiltonian in Eq. 2.9 under PBC.

The corresponding eigenstates are extended, independent from J_R, J_L and can be written as

$$\Psi = \frac{1}{N} \begin{pmatrix} 1 \\ \psi^j \\ \psi^{2j} \\ \vdots \\ \psi^{(N-1)j}, \end{pmatrix} \tag{2.18}$$

where $\psi = e^{\frac{2\pi i}{N}}$.

The Bloch theory fails to exhibit energy spectrum under OBC, as the bulk-boundary correspondence is broken due to the NHSE. Let us find the OBC spectrum and the corresponding OBC modes, known as skin modes. In order to find the spectrum under OBC, we use the non-Bloch theory. Bloch wave number become complex in non-Hermitian systems. Non-Bloch theory states that, we need to determine the Brillouin zone $\beta = e^{ik}$ for the complex k [60, 68]. Using the state, $|\psi\rangle = \sum_n \psi_n \hat{c}_n^\dagger |0\rangle$, the single particle Schrödinger equation $\hat{H} |\psi\rangle = E |\psi\rangle$ leads to the following discrete equations for the complex field amplitude ψ_n at site n

$$J_R \psi_{n-1} + J_L \psi_{n+1} = E\psi_n, \tag{2.19}$$

for $n = 1, \ldots, N$. Imposing OBC by assuming $\psi_0 = \psi_{N+1} = 0$. General solution for Eq. 2.19 is written as

$$\psi_n = (\beta_1)^{(n)} \phi^{(1)} + (\beta_2)^{(n)} \phi^{(2)} \tag{2.20}$$

and eigenvalue equation is

$$E = J_R \beta_i^{-1} + J_L \beta_i, \tag{2.21}$$

where $i = 1, 2$.

Using $\psi_0 = \psi_{N+1} = 0$ in Eq. 2.20 gives

$$\begin{aligned} \psi_0 &= \phi^{(1)} + \phi^{(2)} = 0, \\ \psi_{N+1} &= (\beta_1)^{(N+1)} \phi^{(1)} + (\beta_2)^{(N+1)} \phi^{(2)} = 0. \end{aligned} \tag{2.22}$$

From Eq. 2.22, we see that

$$\left(\frac{\beta_1}{\beta_2}\right)^{N+1} = 1, \tag{2.23}$$

and Eq. 2.23 can be written as

$$\frac{\beta_1}{\beta_2} = e^{2i\theta_j}, \tag{2.24}$$

where $\theta_j = \frac{j\pi}{N+1}$, $m = 1, \cdots, N$ and $|\beta_1| = |\beta_2|$.

Using Eq. 2.21

$$\begin{aligned} J_R\beta_1^{-1} + J_L\beta_1 &= E, \\ J_R\beta_2^{-1} + J_L\beta_2 &= E, \end{aligned} \tag{2.25}$$

we get

$$\beta_1\beta_2 = J_R J_L. \tag{2.26}$$

We say that $r = \sqrt{\frac{J_R}{J_L}}$ and we can write β_i^j as

$$\beta_1^j = re^{i\theta_j}, \quad \beta_2^j = re^{-i\theta_j}. \tag{2.27}$$

Using Eq. 2.27, the eigenvalue equation under OBC becomes

$$E^j = 2\sqrt{J_R J_L}\cos\theta_j. \tag{2.28}$$

These are the energy levels of a system under OBC.

In the thermodynamic limit,

$$\begin{aligned} \beta_1 &= re^{i\theta}, \quad \beta_2 = re^{-i\theta}, \\ E &= 2\sqrt{J_R J_L}\cos\theta, \end{aligned} \tag{2.29}$$

and eigenvalues of OBC spectrum are real and distributed in the interval of [32]

$$[-2\sqrt{J_R J_L}, 2\sqrt{J_R J_L}]. \tag{2.30}$$

$$\textit{plane wave and energy level}: \begin{cases} \beta_1^{(j)} = \sqrt{\frac{J_R}{J_L}} e^{i\theta_j}, \\ \beta_2^{(j)} = \sqrt{\frac{J_R}{J_L}} e^{-i\theta_j}, \\ E^{(j)} = 2\sqrt{J_L J_R}\cos\theta_m, \end{cases} \tag{2.31}$$

where $\left(\theta_j = \frac{j\pi}{N+1},\ j = 1, \ldots, N\right)$

In Eq. 2.17, it can be observed that when $J_R = J_L$, there are no complex eigenvalues under PBC and the system is Hermitian. Otherwise, the system is non-Hermitian and the PBC eigenvalues lie on an ellipse in the complex plane with major, minor radii being $|J_R \pm J_L|$. The corresponding eigenstates are extended. For OBC, eigenvalues lie on the real axis inside the PBC loop as shown in Eq. 2.30.

Fig. 2.2c shows the PBC energy spectrum when Bloch wave vector k goes through the 1D Brillouin zone for $J_R = 0.5$ and $J_L = 1$. Since $J_R^* \neq J_L$, the system shows non-Hermitian behaviour. Eigenvalues of the system has real and imaginary parts. As it can be seen in Fig.2.2c, imaginary part is not symmetric with respect to the Bloch vector while real part remains symmetric with respect to Bloch vector. Asymmetric behaviour of the imaginary part of the eigenvalues arise since probability of the left hopping constant J_L does not equal to probability of the right hopping constant J_R. In addition, Fig.2.2a shows that, PBC spectrum forms a loop on the complex plane while OBC spectrum lie on the real axis. Localized states have real eigenvalues and delocalized states have complex eigenvalues [65]. Thus, while the system under PBC shows delocalized states, the system under OBC shows localized states since the eigenstates under OBC are localized on the edge of the system, showing NHSE [32]. In Fig. 2.2b, eigenvectors for the system under OBC are found to be localized near the left edge of the system. Since $J_L > J_R$, particles have higher probability of hopping to the left than to right. This causes the eigenvectors to tend to localize near the left edge of the system under OBC and we observe NHSE. Also, Fig. 2.2b shows that we cannot observe NHSE if the system is under PBC.

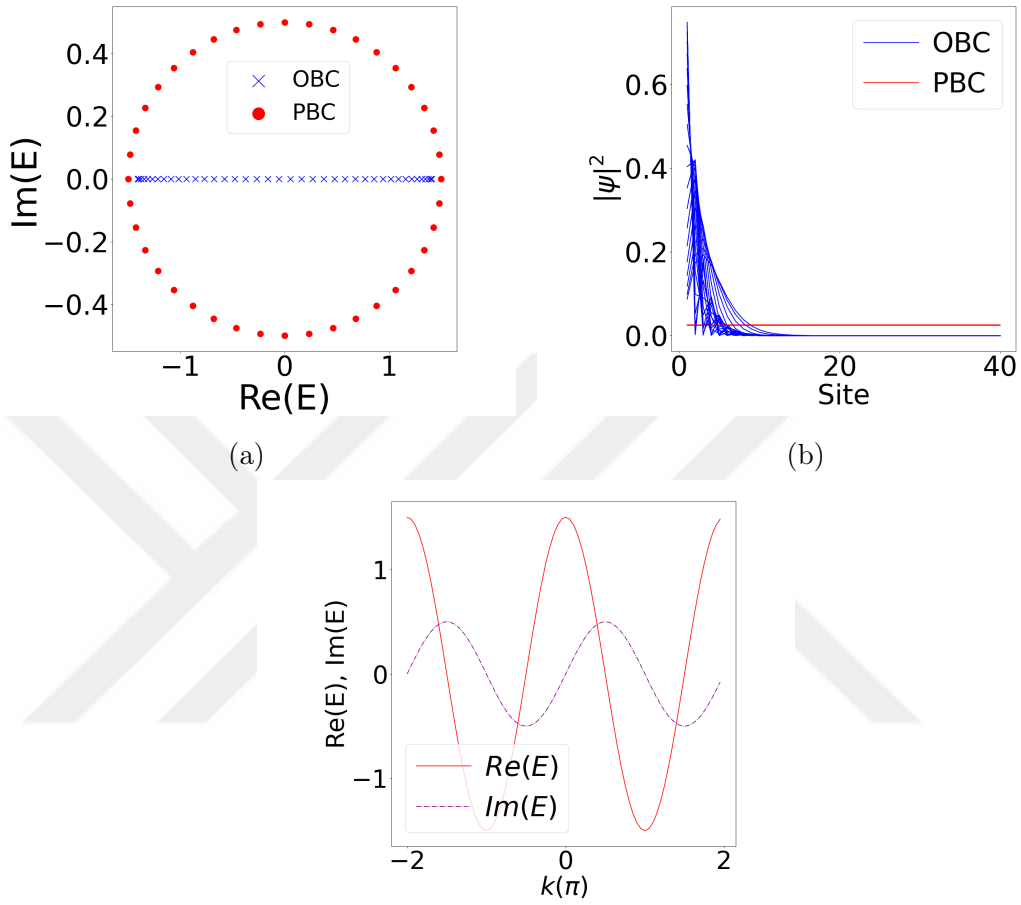

Figure 2.2: Eigenvalues and eigenvectors for the disorder-free HN-model under PBC and OBC when $J_R = 0.5$, $J_L = 1$ and $N = 40$. (a) Eigenvalues under PBC, shown in red dots, form a ellipse on the complex plane with major, minor radii being $|J_R \pm J_L|$. Eigenvalues under OBC, shown in blue crosses, lie on the real axis in the interval of $[-2\sqrt{J_R J_L}, 2\sqrt{J_R J_L}]$. (b) Eigenstates under PBC, shown in red, and OBC, shown in blue, for the disorder-free HN-model. NHSE can be seen in OBC states where the eigenstates are localized at the left edge. (c) Energy spectrum under PBC vs wave vector k.

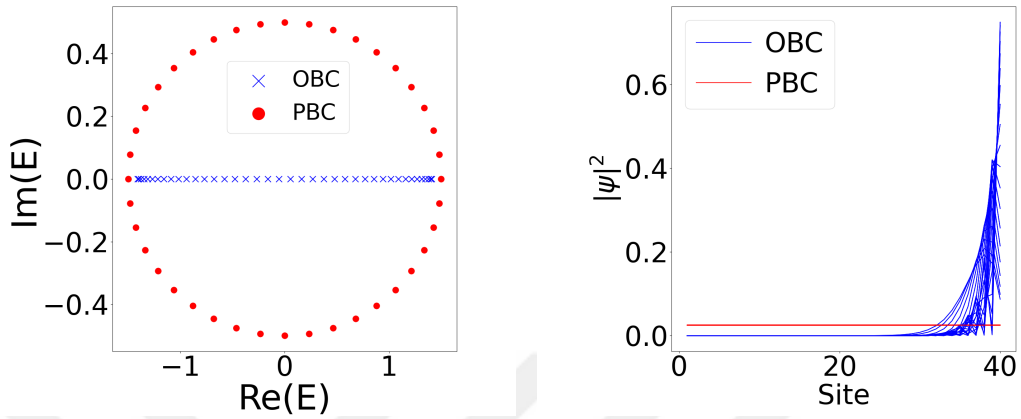

(a)

(b)

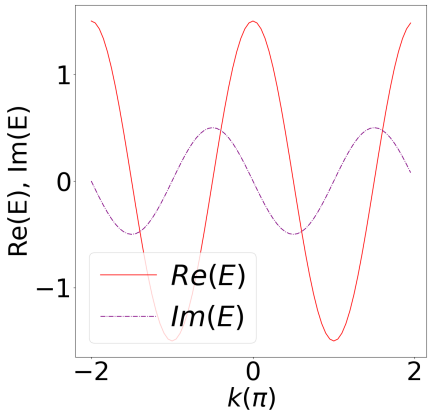

(c)

Figure 2.3: Eigenvalues and eigenvectors for the disorder-free HN-model under PBC and OBC when $J_R = 1$, $J_L = 0.5$ and $N = 40$. (a) Eigenvalues under PBC, shown in red dots, form a ellipse on the complex plane with major, minor radii being $|J_R \pm J_L|$. Eigenvalues under OBC, shown in blue crosses, lie on the real axis in the interval of $[-2\sqrt{J_R J_L}, 2\sqrt{J_R J_L}]$. (b) Eigenstates under PBC, shown in red, and OBC, shown in blue, for the disorder-free HN-model. NHSE can be seen in OBC states where the eigenstates are localized at the right edge. (c) Energy spectrum under PBC vs wave vector k.

Next, we change the hopping constants as shown in Fig. 2.3 as $J_R = 1$ and $J_L = 0.5$ thus making the probability of hopping to the right higher than the probability of hopping to the left. As expected, eigenstates exhibit localization

near the right edge, as depicted in Figure 2.3b. Like in Fig. 2.2c, PBC spectrum shows real symmetric eigenvalues while imaginary part of the eigenvalues are asymmetric with respect to the Bloch vector k. PBC spectrum again forms a loop on the complex energy plane and OBC spectrum lies on the real axis as shown in Fig. 2.3a.

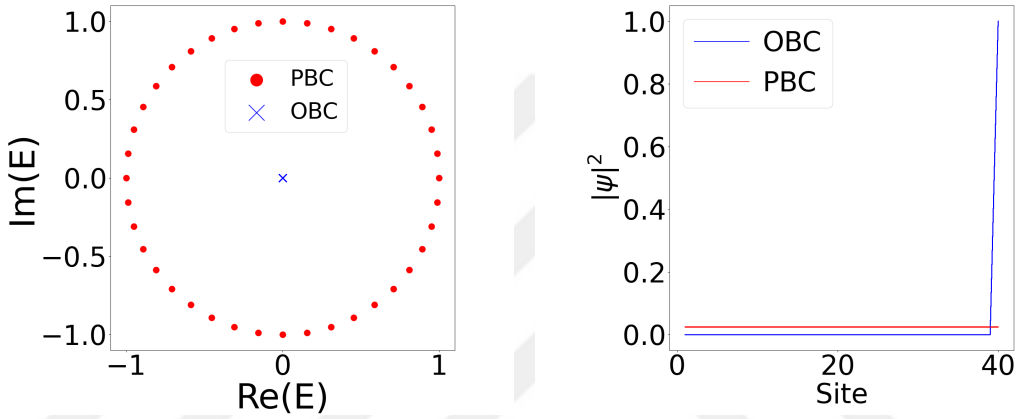

(a)

(b)

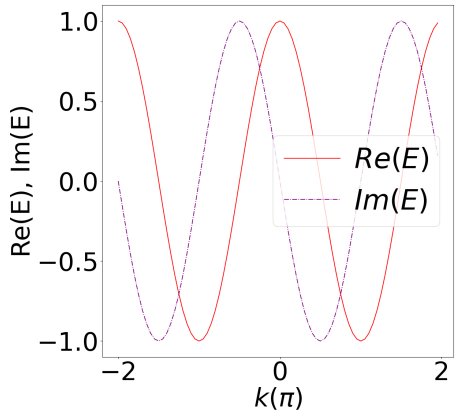

(c)

Figure 2.4: Eigenvalues and eigenvectors for the disorder-free HN-model under PBC and OBC when $J_R = 1$, $J_L = 0$ and $N = 40$. (a) Eigenvalues under PBC form a ellipse on the complex plane while eigenvalues under OBC, coalesce into each other. (b) Eigenstates under PBC, shown in red, and OBC, shown in blue, for the disorder-free HN-model. NHSE can be seen in OBC states where the eigenstates are localized at the right edge, coalescing into each other. (c) Energy spectrum under PBC vs wave vector k.

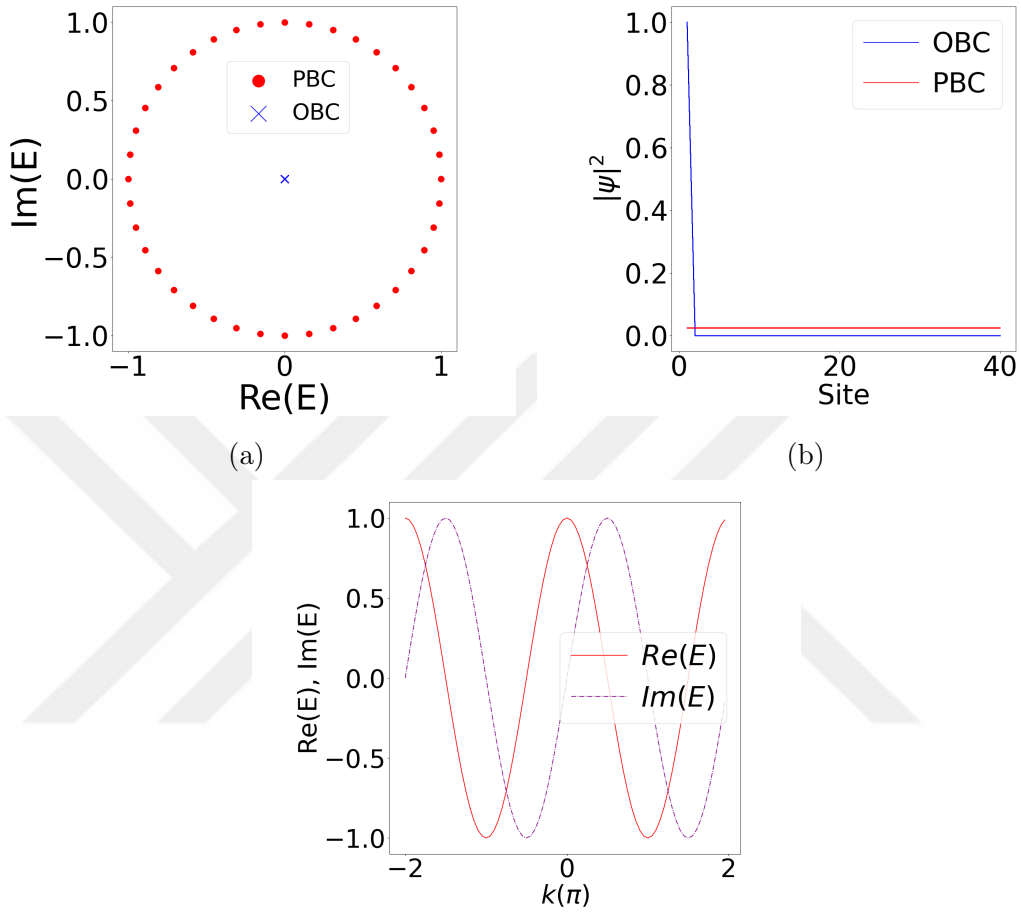

(a) (b)

(c)

Figure 2.5: Eigenvalues and eigenvectors for the disorder-free HN-model under PBC and OBC when $J_R = 0$, $J_L = 1$ and $N = 40$. (a) Eigenvalues under PBC form a ellipse on the complex plane while eigenvalues under OBC, coalesce into each other. (b) Eigenstates under PBC, shown in red, and OBC, shown in blue, for the disorder-free HN-model. NHSE can be seen in OBC states where the eigenstates are localized at the left edge, coalescing into each other. (c) Energy spectrum under PBC vs wave vector k.

Fig. 2.4 and Fig. 2.5 show extreme cases in which one of the hopping constants is zero. In Fig. 2.5c, $J_R = 0$ and $J_L = 1$, the system only allows left hopping, and all eigenstates are localized on the left edge, coalescing into each other and thus having the same eigenvalue. In Fig. 2.4c, $J_R = 1$ and $J_L = 0$, the system

does not allow left hopping, and all eigenstates are localized on the right edge, coalescing into each other and thus having the same eigenvalue.

2.5 Winding number

Topological nature of periodic lattices are quantified by the so-called winding number which can be extracted from E_k as

$$\begin{aligned} w &= \frac{1}{2\pi i}\int_{-\pi}^{\pi} dk \partial_k \ln E_k, \\ &= \frac{1}{2\pi i}\int_{-\pi}^{\pi} \frac{1}{E_k}\frac{\partial E_k}{\partial k}, \end{aligned} \tag{2.32}$$

Substituting Eq. 2.17 into Eq. 2.32 leads to

$$w = \frac{1}{2\pi i}\int_{-\pi}^{\pi} dk \frac{-(J_L+J_R)\sin k + i(J_L-J_R)\cos k}{(J_L+J_R)\cos k + i(J_L-J_R)\sin k}. \tag{2.33}$$

For $J_R = J_L$, i.e., Hermitian case, the winding number vanishes

$$\begin{aligned} w &= \frac{1}{2\pi i}\int_{-\pi}^{\pi} dk \frac{-(J_L+J_R)\sin k}{(J_L+J_R)\cos k}, \\ &= -\frac{1}{2\pi i}\int_{-\pi}^{\pi} dk \tan k, \\ &= 0. \end{aligned} \tag{2.34}$$

Note that $\tan k$ has singularities at $k = \pm\frac{\pi}{2}$. However, since it is an odd function, i.e $\tan -k = -\tan k$, $\int_{-\pi}^{\pi} dk \tan k = 0$ in the interval of $[-\pi, \pi]$. Thus, winding number is zero, $w = 0$. Similarly, at $J_R = -J_L$, $\frac{1}{2\pi i}\int_{-\pi}^{\pi} dk \cot k = 0$.

For $|J_R| \neq |J_L|$, i.e., non-Hermitian case,

$$w = \frac{1}{2\pi i}\int_{-\pi}^{\pi} dk \frac{-(J_L+J_R)\sin k + i(J_L-J_R)\cos k}{(J_L+J_R)\cos k + i(J_L-J_R)\sin k}. \tag{2.35}$$

When $|J_R| < |J_L|$, $w = 1$ and energy spectrum winds around the origin in counterclockwise direction. When $|J_R| > |J_L|$, $w = -1$ and energy spectrum winds around the origin in clockwise direction as shown in Fig. 2.6. At $|J_R| = |J_L|$, there is a transition. NHSE occurs at a non-zero winding number as shown in Fig. 2.2.

$$w = \begin{cases} 1 & \text{if } |J_R| < |J_L|; \\ -1 & \text{if } |J_R| > |J_L|; \\ 0 & \text{if } |J_R| = |J_L|. \end{cases} \tag{2.36}$$

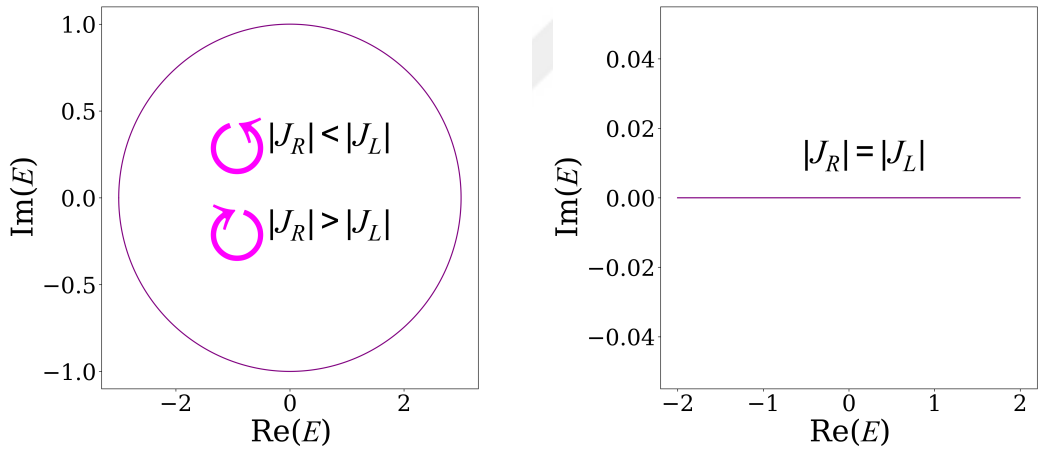

(a) (b)

Figure 2.6: (a) For $|J_R| < |J_L|$, energy spectrum winds around the origin in counterclockwise direction indicating $w = 1$ and for $|J_R| > |J_L|$, energy spectrum winds around the origin in clockwise direction indicating $w = -1$, (b) $w = 0$.

Chapter 3

Scale-free Localization

In Chapter 2, we investigated the Hatano-Nelson model under PBC and OBC and, demonstrated the presence of NHSE. In this chapter, we will analyze the Hatano-Nelson model with generalized boundary conditions (GBC) which is illustrated in Fig. 3.1. GBC behaves as an impurity at the boundaries and gives rise to the formation of scale-free localized (SFL) states. Unlike skin states that are demonstrated in Chapter 2, the localization lengths of the SFL states vary proportionally with the system size, and their spatial profiles remain invariant, regardless of the system size.

The Hamiltonian of the 1D lattice, illustrated in Fig. 3.1 is given by

$$\hat{H} = \sum_{n=1}^{N-1} (J_R \hat{c}_{n+1}^\dagger \hat{c}_n + J_L \hat{c}_n^\dagger \hat{c}_{n+1}) + \zeta_R \hat{c}_1^\dagger \hat{c}_N + \zeta_L \hat{c}_N^\dagger \hat{c}_1, \tag{3.1}$$

where $\hat{c}_n$ ($\hat{c}_n^\dagger$) annihilation(creation) operators at site n, J_R is the hopping constant to the right, J_L is the hopping constant to the left, $J_R^* \neq J_L$ and N is the lattice size. ζ_R and ζ_L determine the GBC.

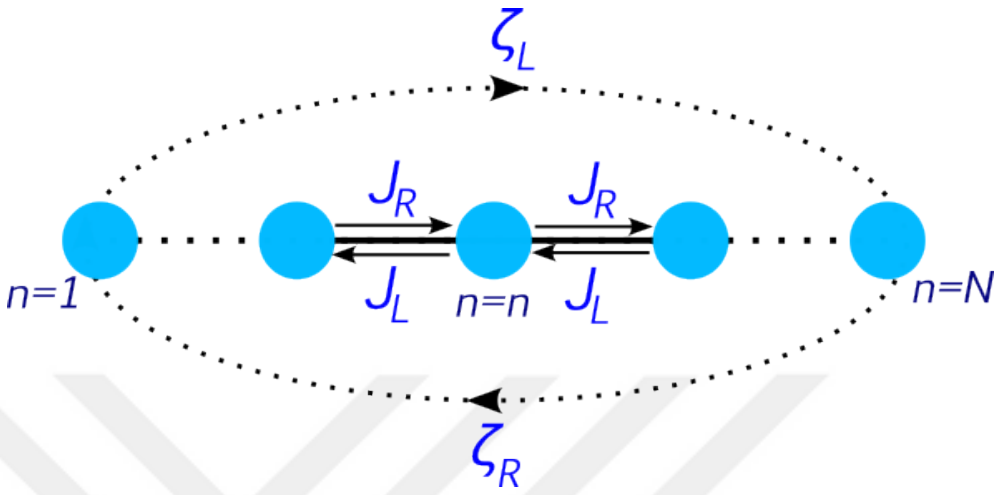

Figure 3.1: 1D non-Hermitian tight-binding Hatano-Nelson model with asymmetric hoppings, $J_R^* \neq J_L$ with Generalized Boundary Conditions.

The corresponding single particle Hamiltonian can be given using bra-ket formalism

$$\hat{H} = \sum_{n=1}^{N-1} (J_R \left|n+1\right\rangle \left\langle n\right| + J_L \left|n\right\rangle \left\langle n+1\right|) + \zeta_R \left|1\right\rangle \left\langle N\right| + \zeta_L \left|N\right\rangle \left\langle 1\right|. \tag{3.2}$$

Its matrix representation of the Hamiltonian reads

$$\mathbf{H} = \begin{pmatrix} 0 & J_L & 0 & \cdots & 0 & 0 & \cdots & 0 & \zeta_R \\ J_R & 0 & J_L & \cdots & 0 & 0 & \cdots & 0 & 0 \\ 0 & J_R & 0 & J_L & 0 & 0 & \cdots & 0 & 0 \\ 0 & 0 & J_R & \ddots & \vdots & \vdots & & \vdots & \vdots \\ \vdots & \vdots & \vdots & & \vdots & & \ddots & \vdots & \vdots \\ 0 & 0 & 0 & \cdots & 0 & 0 & \cdots & 0 & J_L \\ \zeta_L & 0 & 0 & \cdots & 0 & 0 & \cdots & J_R & 0 \end{pmatrix}_{N\times N} . \tag{3.3}$$

The elements ζ_R and ζ_L highlighted in red to show the connections between the first and last sites, imposing GBC.

The eigenvalue equation is given by Schrödinger equation is $\hat{H}\left|\psi\right\rangle = E\left|\psi\right\rangle$,

where $|\psi\rangle$ can be written as a linear combination of the basis states as

$$|\psi\rangle = \sum_n \psi_n \hat{c}_n^\dagger |0\rangle \tag{3.4}$$

where ψ_n describes the probability amplitude of the eigenstate at site n and $|0\rangle$ is the vacuum state for the lattice. Schrödinger equation leads to the following discrete eigenvalue equations for ψ_s at site s, bulk equations (i.e., for non-boundary nodes) can be expressed as

$$J_R\psi_s - E\psi_{s+1} + J_L\psi_{s+2} = 0, \tag{3.5}$$

where $s = 1, \ldots, N-2$. Boundary equations are

$$\begin{aligned} J_L\psi_2 - E\psi_1 + \zeta_R\psi_N &= 0, \\ \zeta_L\psi_1 - E\psi_N + J_R\psi_{N-1} &= 0. \end{aligned} \tag{3.6}$$

Boundary equations can also be expressed as

$$J_R\psi_0 = \zeta_R\psi_N, \quad \zeta_L\psi_1 = J_L\psi_{N+1}. \tag{3.7}$$

Now, we set the general ansatz equation for Eq. 3.5 that satisfies the bulk equations as [69]

$$\Psi = c_1 \begin{pmatrix} z_1 \\ z_1^2 \\ \vdots \\ z_1^N \end{pmatrix} + c_2 \begin{pmatrix} z_2 \\ z_2^2 \\ \vdots \\ z_2^N \end{pmatrix} = \begin{pmatrix} \psi_1 \\ \psi_2 \\ \vdots \\ \psi_N \end{pmatrix}, \tag{3.8}$$

where

$$\Psi_i = \begin{pmatrix} z_i \\ z_i^2 \\ \vdots \\ z_i^N \end{pmatrix}, \tag{3.9}$$

and

$$\psi_n = \sum_{i=1}^{2} (c_i z_i^n) = c_1 z_1^n + c_2 z_2^n, \tag{3.10}$$

where $n = 1, 2, \ldots, N$.

Now, substitute Eq. 3.9 into Eq. 3.5 to get the eigenvalue expression

$$\begin{aligned} J_R z_i^n - E z_i^{n+1} + J_L z_i^{n+2} &= J_R - E z_i + J_L z_i^2, \\ &= \frac{J_R}{z_i} - E + J_L z_i, \\ &= 0. \end{aligned} \tag{3.11}$$

The eigenvalue expression is

$$E = \frac{J_R}{z_i} + J_L z_i. \tag{3.12}$$

When c_1 and c_2 are both zero, there is a trivial solution where Ψ is a zero vector. For nontrivial solutions when $c_1 = 0, c_2 \neq 0$ or $c_1 \neq 0, c_2 = 0$, two solutions of z_i as (z_1, z_2) must follow the below constraint

$$z_1 z_2 = \frac{J_R}{J_L}. \tag{3.13}$$

We now want to show that Ψ_i satisfies the boundary equations that are given in Eq. 3.7. By inserting Eq. 3.9 to Eq. 3.7, we get $H_B(c_1, c_2)^T = 0$

$$\underbrace{\begin{pmatrix} J_R - \zeta_R z_1^N & J_R - \zeta_R z_2^N \\ z_1(\zeta_L - J_L z_1^N) & z_2(\zeta_L - J_L z_2^N) \end{pmatrix}}_{H_B} \begin{pmatrix} c_1 \\ c_2 \end{pmatrix} = 0. \tag{3.14}$$

Taking the determinant of H_B, $\det(H_B) = 0$, we get the general solution as

$$\begin{aligned} &\left(z_1^{N+1} - z_2^{N+1}\right) - \frac{\zeta_R \zeta_L}{t_L^2}\left(z_1^{N-1} - z_2^{N-1}\right) \\ &- \left[\frac{\zeta_L}{J_L} + \frac{\zeta_R}{J_R}\left(\frac{J_R}{J_L}\right)^N\right](z_1 - z_2) = 0. \end{aligned} \tag{3.15}$$

Using $z_1 = re^{i\theta}$, $z_2 = re^{-i\theta}$ and $r = \sqrt{J_R/J_L}$, Eq. 3.15 can be written as

$$\sin[(N+1)\theta] - \eta_1 \sin[(N-1)\theta] - \eta_2 \sin[\theta] = 0, \tag{3.16}$$

where

$$\eta_1 = (\zeta_R \zeta_L / J_R J_L)\,, \qquad \eta_2 = (\zeta_L / J_L)\, r^{-N} + (\zeta_R / J_R)\, r^N. \tag{3.17}$$

Putting $z_1 = re^{i\theta}$, $z_2 = re^{-i\theta}$ in Eq. 3.12 and using $r = \sqrt{J_R/J_L}$

$$\begin{aligned} E = &= \frac{J_R}{re^{i\theta}} + J_L r e^{i\theta} \\ &= J_R \sqrt{\frac{J_L}{J_R}} e^{-i\theta} + J_L \sqrt{\frac{J_R}{J_L}} e^{i\theta} \\ &= \sqrt{J_R J_L}(e^{-i\theta} + e^{i\theta}) \\ &= 2\sqrt{J_R J_L}\cos\theta. \end{aligned} \tag{3.18}$$

Final expression in Eq. 3.18 gives the eigenvalues for the Hatano-Nelson model with GBC. θ is determined by the solutions of the Eq. 3.16 [69].

3.1 Energy Spectrum under GBC

We consider arbitrary ζ_R and ζ_L in the region $0 \leq \frac{\zeta_R}{J_R}, \frac{\zeta_L}{J_L}$. Under GBC, we have complex solutions thus we need to set θ as

$$\theta = \theta_R + i\theta_i. \tag{3.19}$$

Also,

$$\eta_1 = \frac{\zeta_R \zeta_L}{J_R J_L}, \qquad \eta_2 = \frac{\zeta_L}{J_L} r^{-N} + \frac{\zeta_R}{J_R} r^N. \tag{3.20}$$

Insert the new θ expression Eq. 3.19 into Eq. 3.16

$$\sin[(N+1)(\theta_R + i\theta_i)] - \eta_1 \sin[(N-1)(\theta_R + i\theta_i)] - \eta_2 \sin[(\theta_R + i\theta_i)] = 0. \tag{3.21}$$

Using $\sin(x) = \frac{e^{ix}-e^{-ix}}{2i}$ Eq. 3.21 becomes

$$\frac{e^{i[(N+1)(\theta_R+i\theta_i)]} - e^{-i[(N+1)(\theta_R+i\theta_i)]}}{2i} - \eta_1 \frac{e^{i[(N-1)(\theta_R+i\theta_i)]} - e^{-i[(N-1)(\theta_R+i\theta_i)]}}{2i} = \eta_2 \frac{e^{i(\theta_R+i\theta_I)} - e^{-i(\theta_R+i\theta_I)}}{2i}, \tag{3.22}$$

$$e^{i(N+1)(\theta_R+i\theta_I)} - e^{-i(N+1)(\theta_R+i\theta_I)} - \eta_1 \left(e^{i(N-1)(\theta_R+i\theta_I)} - e^{-i(N-1)(\theta_R+i\theta_I)}\right) = \eta_2 \left(e^{i(\theta_R+i\theta_I)} - e^{-i(\theta_R+i\theta_I)}\right). \tag{3.23}$$

In the thermodynamic limit, we can ignore the small terms

$$e^{i(N+1)(\theta_R+i\theta_I)} - \eta_1 e^{i(N-1)(\theta_R+i\theta_I)} = \frac{\eta_2}{e^{-\theta_I} e^{i\theta_R}} \left(1 - e^{-2\theta_I} e^{i2\theta_R}\right), \tag{3.24}$$

$$e^{N\theta_I} e^{\theta_I} e^{-iN\theta_R} e^{-i\theta_R} - \eta_1 e^{N\theta_I} e^{-\theta_I} e^{-iN\theta_R} e^{i\theta_R} = \eta_2 e^{\theta_I} e^{-i\theta_R} \left(1 - \eta_1 e^{-2\theta_I} e^{i2\theta_R}\right), \tag{3.25}$$

$$e^{N\theta_I} e^{\theta_I} e^{-iN\theta_R} e^{-i\theta_R} (1 - \eta_1 e^{-2\theta_I} e^{i2\theta_R}) = \eta_2 e^{\theta_I} e^{-i\theta_R} \left(1 - e^{-2\theta_I} e^{i2\theta_R}\right). \tag{3.26}$$

Assume that $\theta_I > 0$

$$e^{N\theta_I} = \eta_2 e^{iN\theta_R} \frac{\left(1 - e^{-2\theta_I} e^{i2\theta_R}\right)}{\left(1 - \eta_1 e^{-2\theta_I} e^{i2\theta_R}\right)}, \tag{3.27}$$

$$e^{\theta_I} = \sqrt[N]{\eta_2}\, \sqrt[N]{\alpha}, \quad \theta_R = \frac{2\pi j - \theta_\alpha}{N} \tag{3.28}$$

where $\alpha = \frac{1-e^{-2\theta_I} e^{i2\theta_R}}{1-\eta_1 e^{-2\theta_I} e^{i2\theta_R}}$ and θ_α is the angle of the α so that $\alpha = |\alpha| e^{i\theta_\alpha}$.

We stated that $z_1 = re^{i\theta}$, $z_2 = re^{-i\theta}$. Since θ now has complex parts, z_1 and z_2 is written as

$$z_1 = re^{i(\theta_R + i\theta_I)} = \frac{e^{i\theta_R}}{e^{\theta_I}} r, \qquad z_2 = re^{-i(\theta_R + i\theta_I)} = \frac{e^{\theta_I}}{e^{i\theta_R}} r. \tag{3.29}$$

For the $r > 1$ case; $|\alpha|$ is a finite number, $\sqrt[N]{|\alpha|} \to 1$ and $r = \sqrt{J_R/J_L} > 1$ then $J_R > J_L$

$$\eta_2 = \frac{\zeta_L}{J_L} r^{-N} + \frac{\zeta_R}{J_R} r^N \approx \frac{\zeta_R}{J_R} r^N. \tag{3.30}$$

By using Eq. 3.30 in Eq. 3.28 it can be seen that

$$e^{\theta_I} = \sqrt[N]{\frac{\zeta_R}{J_R} r^N} = r \sqrt[N]{\frac{\zeta_R}{J_R}}, \tag{3.31}$$

z_1 and z_2 becomes

$$\begin{aligned} z_1 &\approx \sqrt[N]{\frac{J_R}{\zeta_R}} e^{i\theta_R}, \\ z_2 &\approx \frac{J_R}{J_L} \sqrt[N]{\frac{\zeta_R}{J_R}} e^{-i\theta_R}. \end{aligned} \tag{3.32}$$

When N goes to infinity, we can ignore the small terms

$$|z_1| \approx \sqrt[N]{\frac{J_R}{\zeta_R}} \to 1, \quad |z_2| \approx \frac{J_R}{J_L} \sqrt[N]{\frac{\zeta_R}{J_R}} \to \frac{J_R}{J_L}. \tag{3.33}$$

Eq.3.33 shows that GBC spectrum approaches to that of PBC spectrum in the thermodynamic limit when $r > 1$.

For the $r < 1$ case; $|\alpha|$ is a finite number, $\sqrt[N]{|\alpha|} \to 1$, $r = \sqrt{J_R/J_L} < 1$ then $J_L > J_R$

$$\eta_2 = \frac{\zeta_L}{J_L} r^{-N} + \frac{\zeta_R}{J_R} r^N \approx \frac{\zeta_L}{J_L} r^{-N}. \tag{3.34}$$

By using Eq. 3.34 in Eq. 3.28 it can be seen that

$$e^{\theta_I} = \sqrt[N]{\frac{\zeta_L}{J_L} r^{-N}} = \frac{1}{r} \sqrt[N]{\frac{\zeta_L}{J_L}}, \tag{3.35}$$

z_1 and z_2 becomes

$$\begin{aligned} z_1 &\approx \frac{J_R}{J_L} \sqrt[N]{\frac{J_L}{\zeta_L}} e^{i\theta_R}, \\ z_2 &\approx \sqrt[N]{\frac{\zeta_L}{J_L}} e^{-i\theta_R}. \end{aligned} \tag{3.36}$$

When N goes to infinity, we can ignore the small terms

$$|z_1| \approx \frac{J_R}{J_L} \sqrt[N]{\frac{J_L}{\zeta_L}} \to \frac{J_R}{J_L}, \quad |z_2| \approx \sqrt[N]{\frac{\zeta_L}{J_L}} \to 1. \tag{3.37}$$

Eq.3.37 shows that GBC spectrum approaches to that of PBC spectrum in the thermodynamic limit when $r < 1$.

In order to find the close form of the GBC eigenvalues insert the expressions for z_1 or z_2 in Eq. 3.32 or Eq. 3.36 into the eigenvalue expression in Eq. 3.12

$$E = J_L \sqrt[N]{\frac{\zeta_L}{J_L}} e^{-i\theta_R} + J_R \sqrt[N]{\frac{J_L}{\zeta_L}} e^{i\theta_R} \tag{3.38}$$

It is important to note that Eq. 3.38 shows the size-dependency of the eigenvalues under GBC since the energy spectrum is dependent to the lattice size N. This size-dependent behaviour is characteristic of the SFL states. In Chapter 2, we analyzed the Hatano-Nelson model under PBC ($\zeta_R = J_R$ and $\zeta_L = J_L$) and OBC ($\zeta_R = \zeta_L = 0$) and we stated that unlike SFL states, skin states do not exhibit a size-dependent behaviour, i.e., energy spectrum of skin states is size

independent. This shows us the importance of GBC in determining eigevalues and eigenstates.

3.2 Results and IPR values

In Section 1.1.5, we introduce IPR as a tool for the assessment of the localization of the states. Now, we want to see the relationship between IPR and lattice size under GBC. In Fig. 3.2, hopping constants are chosen as $J_R = 1$ and $J_L = 0.85$ and kept constant while lattice size is increased from $N = 10$ to 80. Fig. 3.2 shows that when lattice size is increased, there is a corresponding decrease in the IPR values, thus the size-dependency of SFL states [69]. We can see this by observing the red areas that are gradually shrinking. Point $a1 - a4$ has IPR values of $0.17, 0.10, 0.05, 0.02$ respectively for $N = 10, 20, 40, 80$. From Fig. 3.3 to Fig. 3.6, the corresponding eigenvalues and eigenvectors of points a_1, a_2, a_3 and a_4 with GBC and as well as PBC and OBC spectrum is shown. Here, it is crucial to note that while the OBC and PBC spectra remain consistent with increasing lattice size, thus showing a size-independent behaviour, GBC spectrum changes with increasing lattice size, showing a size-dependent behaviour.

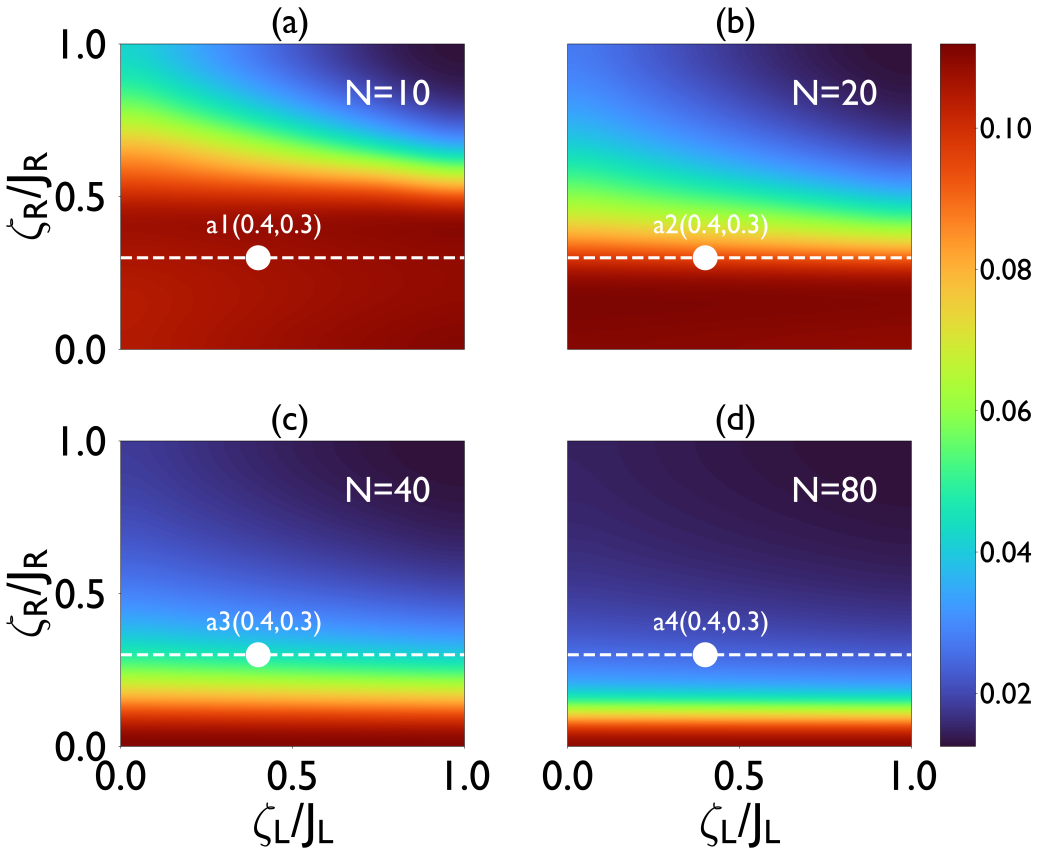

Figure 3.2: IPR values are plotted as a function of ζ_R and ζ_L for (a) $N = 10$, (b) $N = 20$, (c) $N = 40$ and (d) $N = 80$. Common parameters are $J_R = 1$ and $J_L = 0.85$. When lattice size is increasing, there is a corresponding decrease in the IPR value.

Fig. 3.3 shows the eigenvalues and eigenvectors of the point a_1 in Fig. 3.2(a) under PBC, OBC and GBC. Eigenvalues are all real like the OBC spectrum meaning that corresponding eigenstates are localized. However, as we mentioned before, if localization length is larger than the system size, we observe the corresponding state as delocalized state. IPR value that is on the order of $1/N$ indicates delocalized states. Here, even though the states are localized IPR value of point $a1$ is 0.17, since the localization length is larger than the system size.

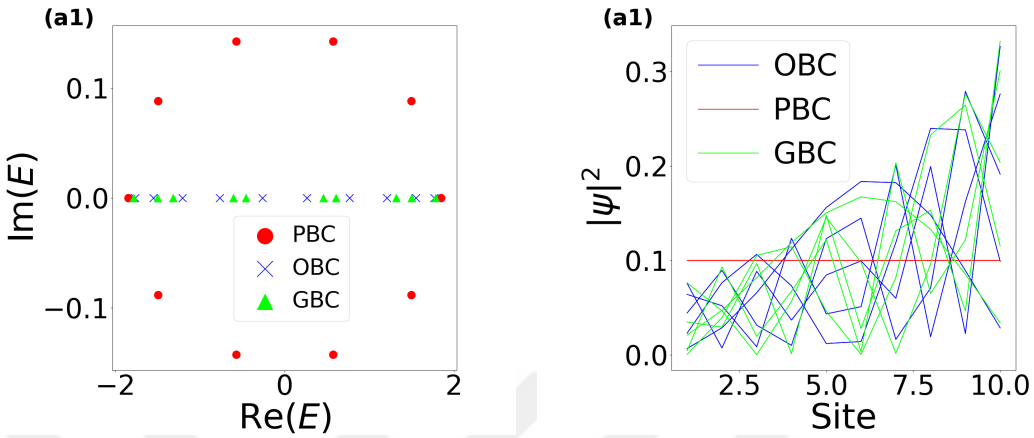

(a) (b)

Figure 3.3: PBC, OBC and GBC cases are shown in red, blue and lime respectively. (a) eigenvalues of $a1$, (b) eigenvectors of $a1$.

In Fig. 3.4a, eigenvalues under GBC begin to exhibit imaginary eigenvalues, thus they start to form a loop on the complex plane. IPR is in the order of 1/20 (0.05). In Fig. 3.5a formation of this loop on the complex plane continues. IPR decreases to the order of 1/40 (0.025). By the time we consider a system size of $N = 80$, the GBC spectrum almost coincides with it PBC spectrum as shown in Fig. 3.6a. IPR reduces to order of 1/80 (0.0125).

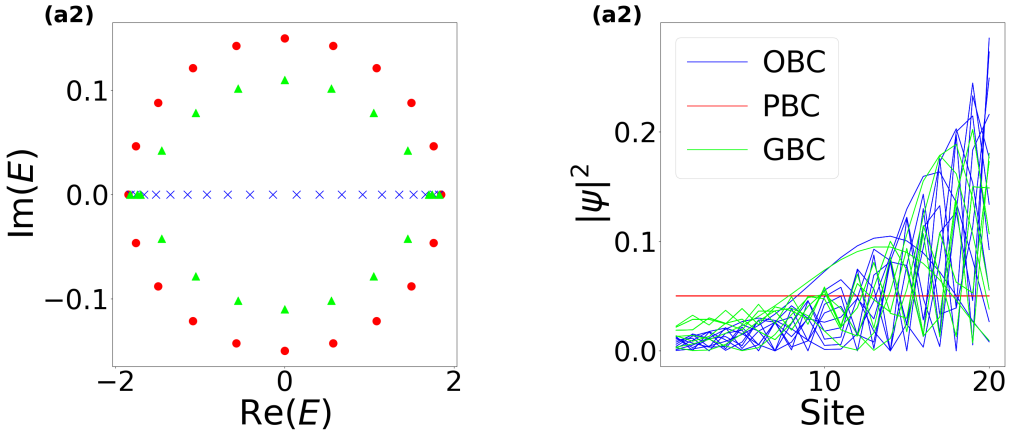

(a) (b)

Figure 3.4: PBC, OBC and GBC cases are shown in red, blue and lime respectively. (a) eigenvalues of $a2$, (b) eigenvectors of $a2$.

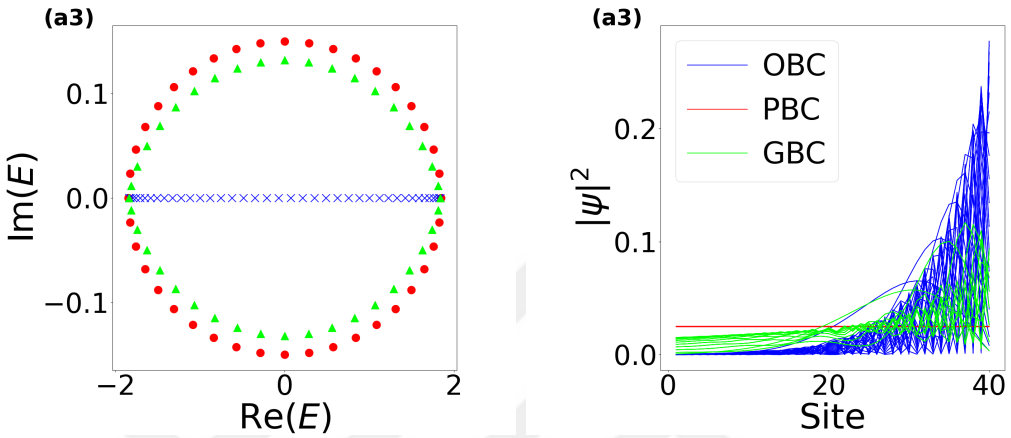

(a) (b)

Figure 3.5: PBC, OBC and GBC cases are shown in red, blue and lime respectively. (a) eigenvalues of $a3$, (b) eigenvectors of $a3$.

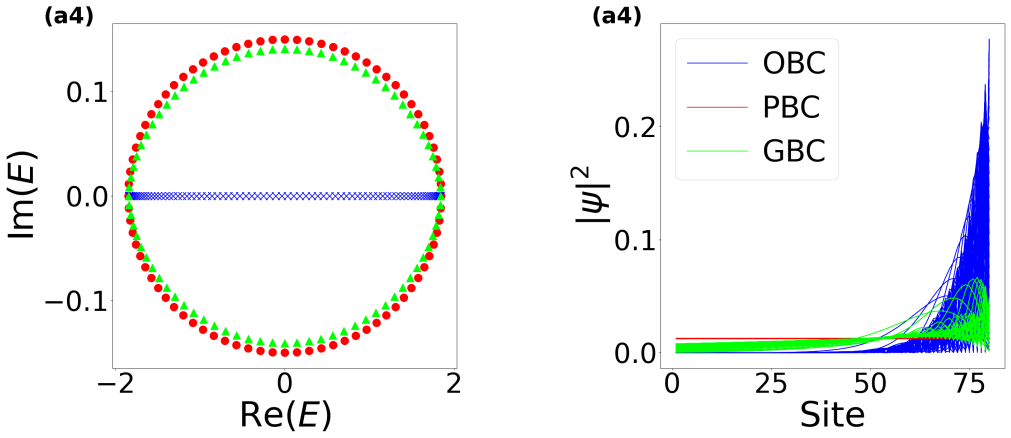

(a) (b)

Figure 3.6: PBC, OBC and GBC cases are shown in red, blue and lime respectively. (a) eigenvalues of $a4$, (b) eigenvectors of $a4$.

Chapter 4

Anderson Localization in non-Hermitian Systems: The Hatano-Nelson Model

In this chapter, we study the Hatano-Nelson model to explore Anderson localizations in non-Hermitian systems.

Random potentials introduced throughout an otherwise periodical lattice cause scatterings and disruption of wave diffusion. As reasoned by Anderson, charge or spin transport behaviour in disordered lattices can remarkably change from that of a periodic one having extended wave functions. The excitations can get trapped in the vicinity of impurities and cease to diffuse, causing their localization. This disorder-driven phenomenon is known as Anderson localization [31].

4.1 Introducing Disorder

We consider the one-dimensional and a one-band lattice model with asymmetric hopping amplitudes and random on-site potentials, depicted in Fig. 4.1. The

Hamiltonian is given by

$$\hat{H} = \sum_{n=1}^{N} (J_R \hat{c}_{n+1}^{\dagger} \hat{c}_n + J_L \hat{c}_n^{\dagger} \hat{c}_{n+1}) + \sum_{n=1}^{N} V_n \hat{c}_n^{\dagger} \hat{c}_n, \tag{4.1}$$

where $\hat{c}_n$ ($\hat{c}_n^{\dagger}$) annihilation (creation) operators at site n, J_R is the hopping constant to the right, J_L is the hopping constant to the left with $J_R^* \neq J_L$, N is the lattice size and V_n represents random uncorrelated on-site energies uniformly distributed in the interval of $W[-0.5, 0.5]$ with W being the disorder strength. To impose PBC, assume that $n = 1$ coincides with $n = N + 1$ ($\hat{c}_1 = \hat{c}_{N+1}$).

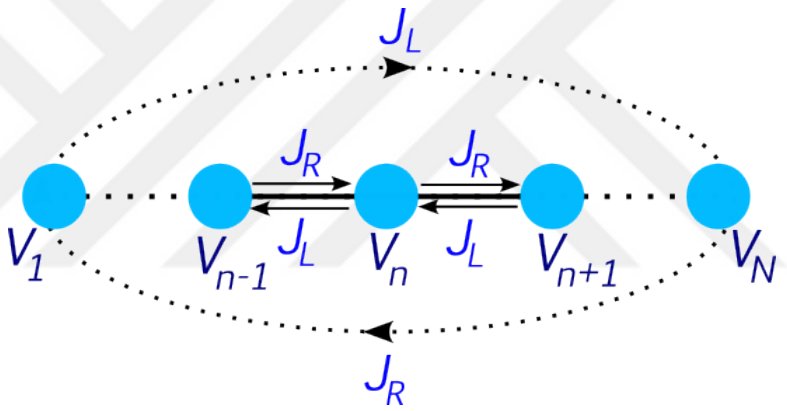

Figure 4.1: Introducing random on-site potentials to 1D non-Hermitian tight-binding Hatano-Nelson model with asymmetric hoppings, $J_R^* \neq J_L$.

We can rewrite Eq. 4.1 without using second-quantized operators as

$$\hat{H} = \sum_{n=1}^{N} (J_R \left|n+1\right\rangle \left\langle n\right| + J_L \left|n\right\rangle \left\langle n+1\right|) + \sum_{n=1}^{N} V_n \left|n\right\rangle \left\langle n\right|. \tag{4.2}$$

and its matrix representation is given by

$$\begin{pmatrix} V_1 & J_L & 0 & \cdots & 0 & 0 & \cdots & 0 & J_R \\ J_R & V_2 & J_L & \cdots & 0 & 0 & \cdots & 0 & 0 \\ 0 & J_R & V_3 & J_L & 0 & 0 & \cdots & 0 & 0 \\ 0 & 0 & J_R & \ddots & \vdots & \vdots & & \vdots & \vdots \\ \vdots & \vdots & \vdots & & \vdots & & \ddots & \vdots & \vdots \\ 0 & 0 & 0 & \cdots & 0 & 0 & \cdots & V_{N-1} & J_L \\ J_L & 0 & 0 & \cdots & 0 & 0 & \cdots & J_R & V_N \end{pmatrix}_{N\times N} \tag{4.3}$$

The elements J_R and J_L that are highlighted in red show the connections between the first and last sites, imposing PBC. They become zero when the system is under OBC. This matrix will be used to find the eigenvalues and eigenvectors in numerical calculations of the 1D lattice with asymmetric hopping amplitudes and random on-site potentials.

4.2 Competition Between NHSE and Anderson Localization

Disorder causes Anderson localization. All states become Anderson localized states with sufficiently strong disorder strength, W. This sufficiently strong W is referred to as the critical disorder strength W_c which is the point where the Anderson transition occurs meaning all states are Anderson localized [70]. Quantitatively it is identified by the value of W at which the energy spectra of a lattice under both PBC and OBC coalesce to the real axis. Fig. 4.2 shows the competition between NHSE and Anderson localization. We will observe the behaviour of the eigenstates for increasing disorder strength W while keeping $J_R = 0.5$ and $J_L = 1$ fixed.

- When there is no disorder, $W = 0$, system keeps its asymmetry and exhibits a dominance of NHSE through out the lattice [70]. Fig. 4.2a shows the

disorder-free case where all eigenvectors are localized near the left edge of the lattice since $J_L > J_R$.

- When disorder is introduced to the system, states start to become Anderson localized states. For a moderately strong disorders such as $W = 2$ and $W = 4$ in Fig. 4.2b and Fig. 4.2c, NHSE and Anderson localized states coexist.

- When W is strong, the system mainly exhibits Anderson localization. In Fig. 4.2d, where the disorder strength is chosen as $W = 6$, the states are Anderson localized.

In Fig. 4.3, we show the corresponding eigenvalues of the eigenstates in Fig.4.2. In the disorder-free case, ($W = 0$), the PBC spectrum forms a loop on the complex plane. When disorder is introduced into the system, the eigenvalues start to coalesce onto the real axis, and the loop deforms. Fig. 4.3d shows the Anderson transition point at $W_c = 6$ where both PBC and OBC spectra fall into the real axis.

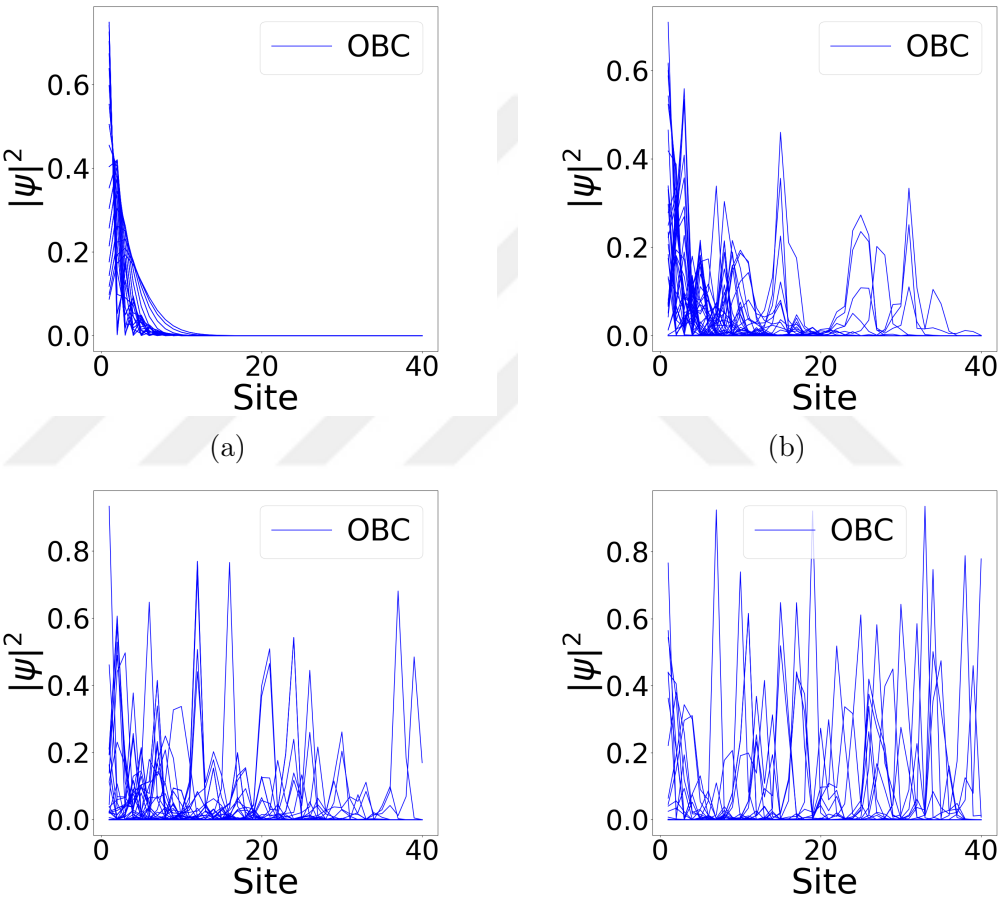

Figure 4.2: Eigenstates under OBC for $J_R = 0.5$, $J_L = 1$, $N = 40$ and different disorder strengths: (a) $W = 0$, NHSE; (b) $W = 2$, coexistence of NHSE and Anderson localization; (c) $W = 4$, coexistence of NHSE and Anderson localization; (d) $W = 6$, Anderson localization.

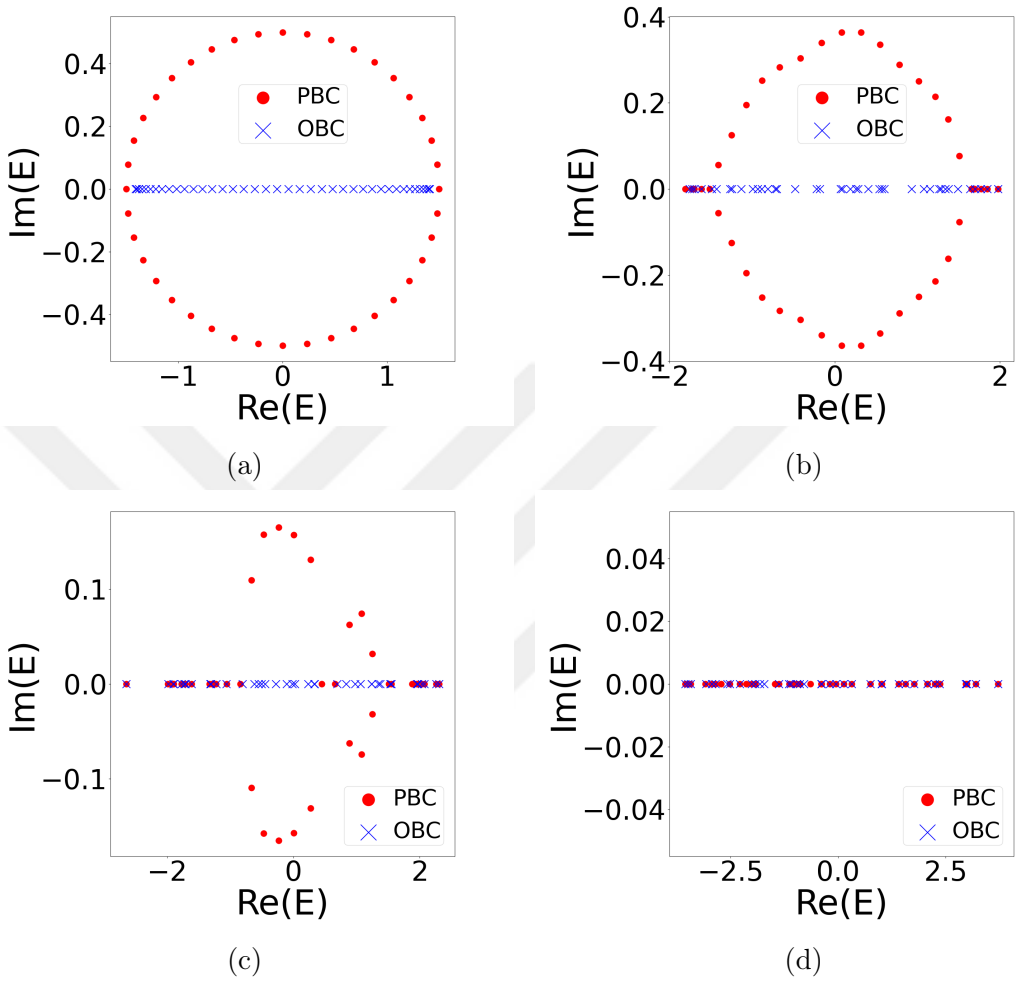

Figure 4.3: Eigenvalues corresponding to Fig. 4.2 under OBC (blue) and PBC (red) for $J_R = 0.5$, $J_L = 1$, $N = 40$, and various disorder strengths: (a) $W = 0$, the PBC spectrum forms a loop in the complex energy plane while OBC loops lie on the real axis; (b) $W = 2$, the PBC loop begins to deform; (c) $W = 4$, the PBC loop continues deforming; (d) $W = 6$, both the PBC and OBC spectra lie on the real axis, and the corresponding states are Anderson localized.

As another example, Fig. 4.4 shows the energy spectrum under PBC of a lattice size $N = 1000$. As expected, PBC forms a loop and this loop starts to deform with the introduction and increasing of disorder W. Critical disorder strength is found to be $W_c = 5$ since the energy spectrum lie on the real axis and all eigenstates are Anderson localized.

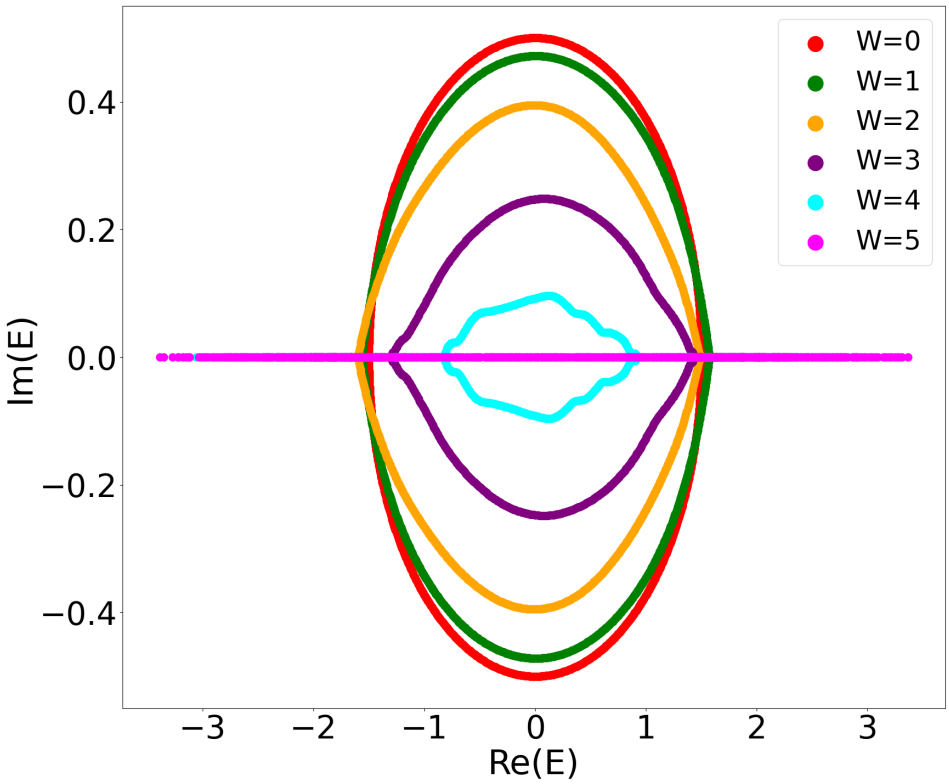

Figure 4.4: Eigenvalues under PBC for $N = 1000$ and different disorder strenghts.

It is important to emphasize that, although W_c is found to be 5 for $N = 1000$ and 6 for $N = 40$, the critical disorder strength is not dependent on lattice size in the Hatano-Nelson model. The difference between $N = 40$ and $N = 1000$ is due to the use of random potentials. If the results are averaged over many potential realizations, this difference will disappear. Thus, now we want to observe the relationship between the critical disorder strength W_c and lattice size N. In order to observe this relationship, W_c is determined for $N = 40, 80, 160$ and 1000. Results are averaged over 10000 potential realizations. Table 4.1 shows that as the lattice size increases, there is no significant corresponding increase or decrease in W_c. While there is a slight difference in the W_c values, this difference is to disappear if the results are averaged over more potential realizations. This indicates a size-independent Anderson localization. With the introduction

of disorder NHSE states transform into Anderson localized states. Localization length of NHSE states are size-independent, thus a size-independent Anderson localization is expected in such a system. We will observe size-dependent Anderson localization in Chapter 6.

N	40	80	160	1000
W_c	5.54	5.51	5.52	5.48

Table 4.1: Relationship between critical disorder strength W_c and lattice size N in the Hatano-Nelson model. The results show no size dependency.

Chapter 5

1D Hermitian Lattice with a non-Hermitian Impurity and Scale Free Localization

In this chapter, we will observe and analyze the behavior of scale-free localized (SFL) states in a 1D Hermitian Lattice with a non-Hermitian Impurity. When a local non-Hermitian impurity is introduced into a Hermitian lattice, scale-free localization occurs. As we mentioned in Chapter 3, the spatial decay length of SFL states is not fixed and scales with the size of the system while the profile of SFL states is not dependent on the size, thus the name scale-free. In other words, when the size of the system is rescaled, eigenstates keep their profile and shape. This differs from the skin states where the localization length is independent of the size of the system [51, 57]. In Chapter 6, we will add disorder to the system and observe the coexistence of SFL and Anderson localization.

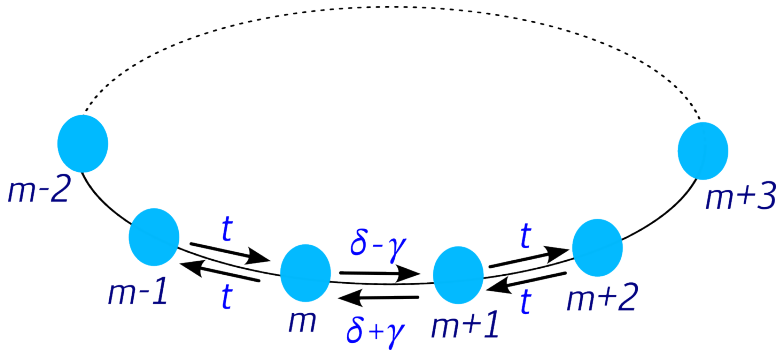

Figure 5.1: 1D Hermitian lattice with a non-Hermitian impurity. t's are the Hermitian hoppings between the neighboring sites and non-Hermitian impurity at site m has $\delta - \gamma$ to the right and $\delta + \gamma$ to the left.

5.1 The Model

In order to achieve this, we will first make the lattice Hermitian by setting $J_R = J_L = t$, and then add a non-Hermitian impurity to the lattice when there is no disorder.

As illustrated in Fig. 5.1, the Hamiltonian is given by

$$\hat{H} = \sum_{n \neq m} t(\hat{c}^\dagger_{n+1}\hat{c}_n + \text{H.c.}) + (\delta - \gamma)\hat{c}^\dagger_{m+1}\hat{c}_m + (\delta + \gamma)\hat{c}^\dagger_m\hat{c}_{m+1}, \tag{5.1}$$

where t is the hopping constant between neighbouring sites, $\hat{c}_n$ ($\hat{c}^\dagger_n$) annihilation(creation) operators at site n, δ and γ define the local non-Hermitian impurity at site m and $\gamma, \delta, W \in \mathbb{R}$. For PBC, assume that $\hat{c}_{N+1} = \hat{c}_1$. We will set $t = 1$ for simplicity.

We can rewrite Eq.5.1 for PBC without using second quantized operators and in bra-ket notation

$$\begin{aligned}\hat{H}_{\text{PBC}} = &\sum_{n=1}^{N-1} t(|n\rangle\langle n+1| + |n+1\rangle\langle n|) + t(|N\rangle\langle 1| + |1\rangle\langle N|) \\ &+ (\delta - \gamma)|m+1\rangle\langle m| + (\delta + \gamma)|m\rangle\langle m+1|.\end{aligned} \tag{5.2}$$

Matrix representation of the model is as follows

$$\begin{pmatrix} 0 & t & 0 & \cdots & 0 & 0 & \cdots & 0 & t \\ t & 0 & t & \cdots & 0 & 0 & \cdots & 0 & 0 \\ \vdots & \vdots & \vdots & \ddots & 0 & \delta+\gamma & \cdots & & \vdots \\ \vdots & \vdots & \vdots & & \delta-\gamma & 0 & \cdots & & \vdots \\ \vdots & \vdots & \vdots & & \vdots & & \ddots & \vdots & \vdots \\ 0 & 0 & 0 & \cdots & 0 & 0 & \cdots & 0 & t \\ t & 0 & 0 & \cdots & 0 & 0 & \cdots & t & 0 \end{pmatrix}_{N\times N} \tag{5.3}$$

where non-Hermitian impurities are highlighted in blue: $\delta-\gamma$ and $\delta+\gamma$, PBC is satisfied with the red t's. This matrix will be used to find eigenvalues and eigenvectors in numerical calculations of the 1D lattice with a non-Hermitian impurity model.

The eigenvalue equation is given by $\hat{H}\left|\psi\right\rangle = E\left|\psi\right\rangle$, where $\left|\psi\right\rangle$ can be written as a linear combination of the basis states as

$$\left|\psi\right\rangle = \sum_n \psi_n \hat{c}_n^\dagger \left|0\right\rangle \tag{5.4}$$

where ψ_n describes the probability amplitude of the eigenstate at site n.

Eigenvalue equation for $n \neq m, m+1$

$$t\psi_{n+1} + t\psi_{n-1} = E\psi_n. \tag{5.5}$$

Eigenvalue equations for the impurity sites are

$$\begin{aligned} t\psi_{m-1} + (\delta+\gamma)\psi_{m+1} &= E\psi_m, \\ t\psi_{m+2} + (\delta-\gamma)\psi_m + &= E\psi_{m+1}. \end{aligned} \tag{5.6}$$

In Hermitian systems, bulk states are known to be insensitive to the local Hermitian impurities except for a few impurity-induced bound states [71]. It is important to ask whether local non-Hermiticity can cause drastic changes to the original Hermitian systems. Non-Hermitian impurity as in Fig.5.1 is induced to the 1D lattice.

The energy spectrum for disorder-free system that is given in Eq. 5.1 under PBC and OBC have spectral differences where PBC spectrum may form a loop on the complex energy plane and OBC spectrum lies on the real axis. This difference leads to the formation of SFL states under PBC. A single non-Hermitian impurity results in the emergence of a significant number of SFL states.

5.2 Distinct Parameter Regions

The disorder-free system exhibits intriguing symmetry properties [71]. The impurity strengths δ and γ determine the PT symmetry of the system. By varying them, the system transitions through the PT-unbroken, PT-broken, and PT-restoration regions as shown in Fig. 5.2. As PT-symmetry varies, extended and bulk states transform into SFL states [71].

1. PT-unbroken region where $\gamma < |\delta - t|$
2. PT-broken region where $|\delta - t| < \gamma < \delta + t$
3. PT-restoration region where $\gamma > \delta + t$

In Fig. 5.2, the number of complex eigenvalues is plotted as a function of δ and γ. Points a to d are selected for a detailed analysis of the system's eigenvalues and eigenvectors. We will examine the figure in three distinct regions: PT-unbroken, PT-broken, and PT-restoration.

In Fig.5.3-5.7, the color codes are assigned based on the IPR values of the eigenstates of Eq. 5.1. We use the following algorithm to assign the color codes:

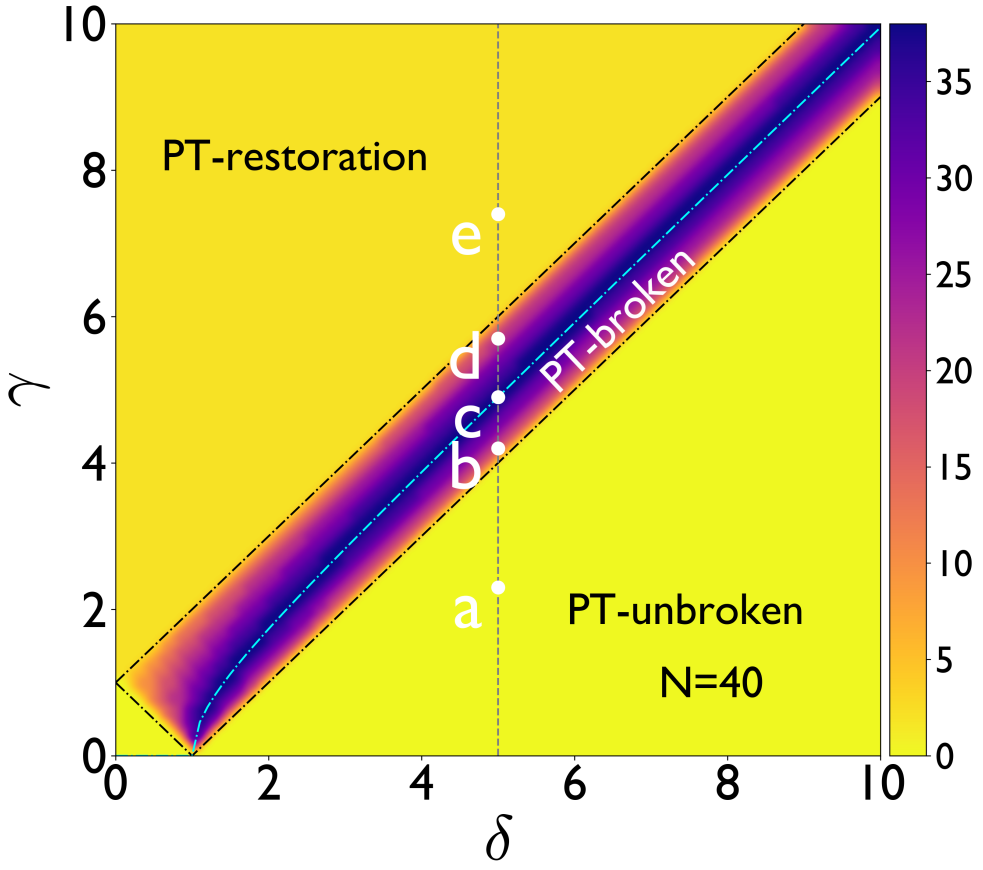

Figure 5.2: Phase diagram of the 1D lattice described by Eq. 5.1 for the disorder-free case. The lattice size is $N = 40$, $t = 1$, and the impurity is positioned at $m = 20$. The color map represents the number of complex eigenvalues. The cyan line, where $\gamma = \sqrt{\delta^2 - t^2}$, indicates the transition to SFL states for all states. The black dashed lines, given by $\gamma = |\delta - t|$ and $\gamma = \delta + t$, represent the phase boundaries of PT-symmetry for there regions: PT-unbroken region where $\gamma < |\delta - t|$, PT-broken region where $|\delta - t| < \gamma < \delta + t$, PT-restoration region where $\gamma > \delta + t$. Points a to e lie along the vertical axis where $\delta = 5t$.

- Bound states are generally localized and have high IPR values. For our case, bound states are caused by the impurity. These impurity-bound states have real energies in PT-unbroken region and complex energies in PT-restoration region. Bound states and corresponding eigenvalues are highlighted in blue.
- Extended bulk states are delocalized states that spreads through out the lattice. These states have low IPR values. Extended states and corresponding states are highlighted in magenta.
- Localization length of the SFL states scales with the system size and IPR values of SFL states are between those of bound and extended states. SFL states and corresponding eigenvalues are highlighted in lime.

5.3 Results

In the PT-unbroken region, where $\gamma < |\delta - t|$, the system has extended bulk states and two impurity-bound states with real eigenvalues under both PBC and OBC. Fig. 5.3 shows the eigenvalues and eigenvectors of point a under PBC. In this region, there are two impurity-bound states and extended bulk states with real eigenvalues. Energy spectrum is entirely real. There are no SFL states in PT-unbroken region. Since SFL states often emerge with the broken PT symmetry. It is noteworthy that although the Hamiltonian is non-Hermitian, energy spectrum is real indicating PT-symmetry is preserved.

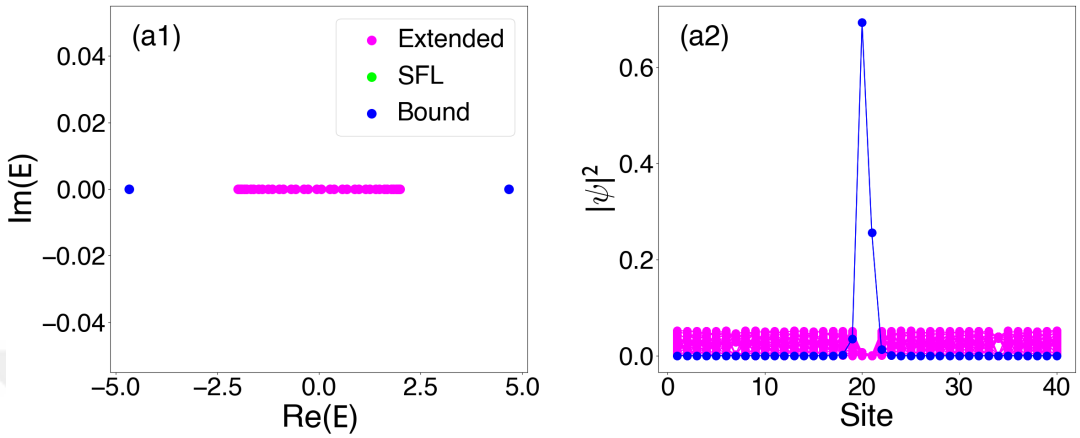

Figure 5.3: (a1) Eigenvalues and (a2) Eigenvectors of the PT-unbroken region. Eigenvalues and eigenvectors are categorized as follows: extended bulk states with real eigenvalues (magenta) and two impurity-bound states with real eigenvalues (blue).

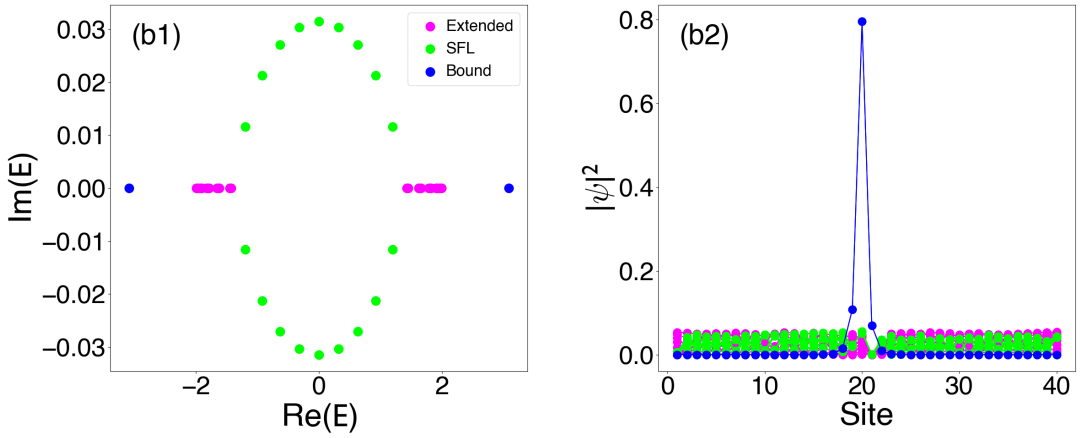

Figure 5.4: (b1) Eigenvalues and (b2) Eigenvectors of the PT-broken region. Eigenvalues and eigenvectors are categorized as follows: extended states with real eigenvalues (magenta), two impurity-bound states with real eigenvalues (blue) and SFL states forming a loop on the complex plane (lime).

When γ surpasses $|\delta - t|$, the system no longer preserves PT symmetry and enters to the PT-broken region. In PT-broken region, the PBC spectrum begins to exhibit complex eigenvalues starts to form a loop on the complex energy plane. This leads to the emergence of the SFL states. In Fig. 5.4, the system is now in PT-broken region. We observe the coexistence of extended and bound states with real eigenvalues and SFL states starting to form a loop on the complex plane. The localization lengths of the SFL states vary proportionally with the size of the system while spatial profiles of the states remain independent of the system size. It is important to mention that this coexistence of bound, extended and SFL states continues until $\gamma = \sqrt{\delta^2 - t^2}$ as shown in Fig. 5.5. Note that extended and SFL states coexist in the system, and all eigenstates become SFL states at $\gamma = \sqrt{\delta^2 - t^2}$ [8]. In Fig. 5.6, system still is in PT-broken region and we observe the coexistence of extended, bound and SFL states since the point d is above the $\gamma = \sqrt{\delta^2 - t^2}$ curve. Extended states have real eigenvalues but in this point, impurity-bound states have complex eigenvalues and loop that SFL states forms in the complex plane starts to lie on the real axis.

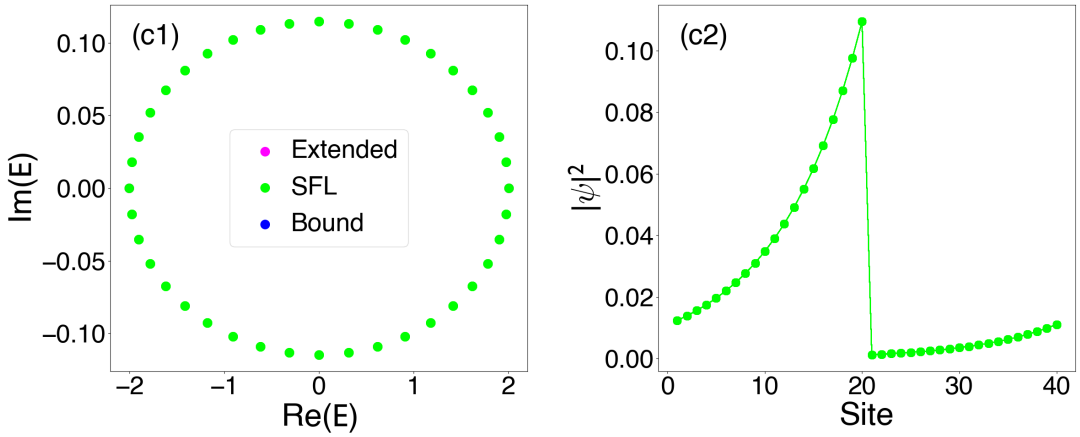

Figure 5.5: (c1) Eigenvalues and (c2) Eigenvectors of the PT-broken region. Eigenvalues and eigenvectors are categorized as follows: SFL states form a loop on the complex plane (lime).

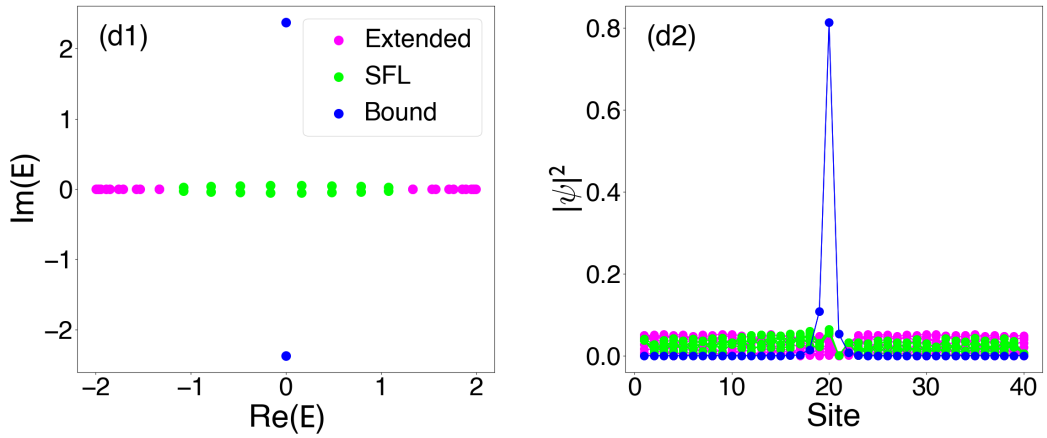

Figure 5.6: (d1) Eigenvalues and (d2) Eigenvectors of the PT-broken region. Eigenvalues and eigenvectors are categorized as follows: extended states with real eigenvalues (magenta), two impurity-bound states with complex eigenvalues (blue) and SFL states with real and complex eigenvalues (lime).

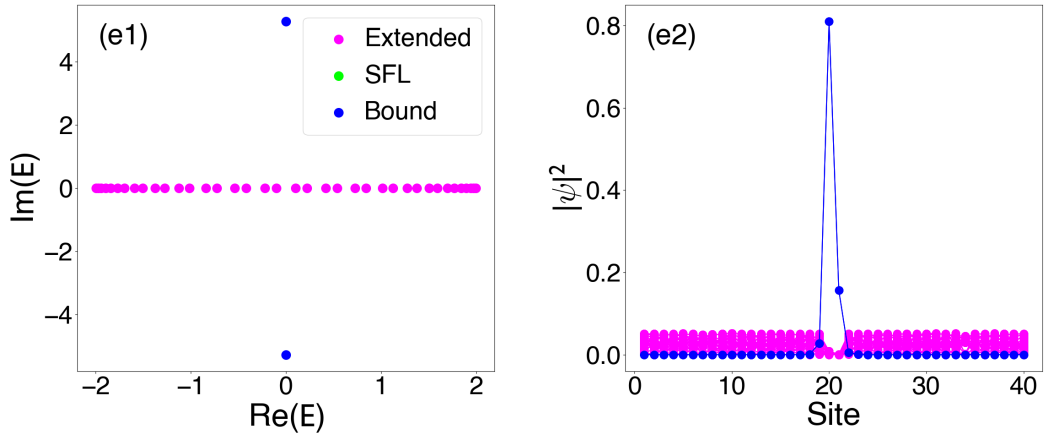

Figure 5.7: (e1) Eigenvalues and (e2) Eigenvectors of the PT-restoration region. Extended states with real eigenvalues and two impurity-bound states with complex eigenvalues.

When γ is increased enough to exceed $|\delta + t|$, system enters the PT-restoration

region. In this region, SFL states disappear since the emergence of SFL states are related to broken PT symmetry. There are two impurity-bound states with complex eigenvalues and extended states with real eigenvalues in PT-restoration region as shown in Fig. 5.7.

In order to show that the spatial profile of the SFL states is independent of the lattice size, we now will compare the $N = 40$ case with the extreme case $N = 1000$. Fig. 5.8 shows that the localization length of SFL states scales with the system size.

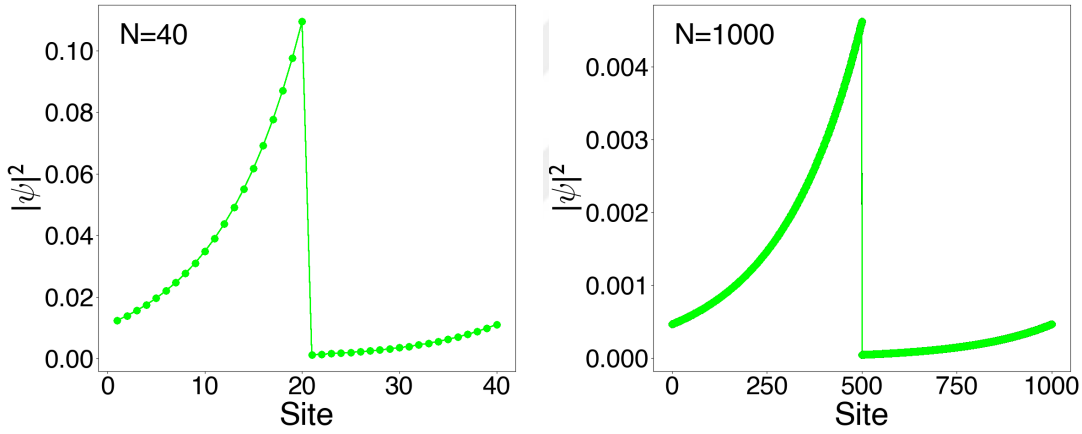

(a) (b)

Figure 5.8: Eigenstates when $\gamma = \sqrt{\delta^2 - t^2}$ for lattice sizes (a) $N = 40$ and (b) $N = 1000$. Impurity is positioned at $m = N/2$.

As an example and to analyze the energy spectrum in more detail, energy spectra with respect to γ for $\delta = 5t$ which is the gray line in Fig. 5.2 is shown in Fig. 5.9. As we discussed above in detail, when $\gamma < |\delta - t|$ which in case $\gamma < 4$, system is in PT-broken region. There are two real eigenvalues corresponding to two impurity-bound states and $N - 2$ real eigenvalues corresponding to extended bulk states. Increasing γ to exceed $|\delta - t|$, system enters the PT-broken region. The number of real eigenvalues starts to decrease, reach its minimum value at the cyan line in Fig. 5.2 which is $\gamma = \sqrt{\delta^2 - t^2}$ and start to increase when it passes this line. When γ is increase to exceed $\delta + t$, system enters the PT-restoration region

and regains the extended bulk states with real eigenvalues. In PT-restoration region, impurity-bound states now have imaginary eigenvalues.

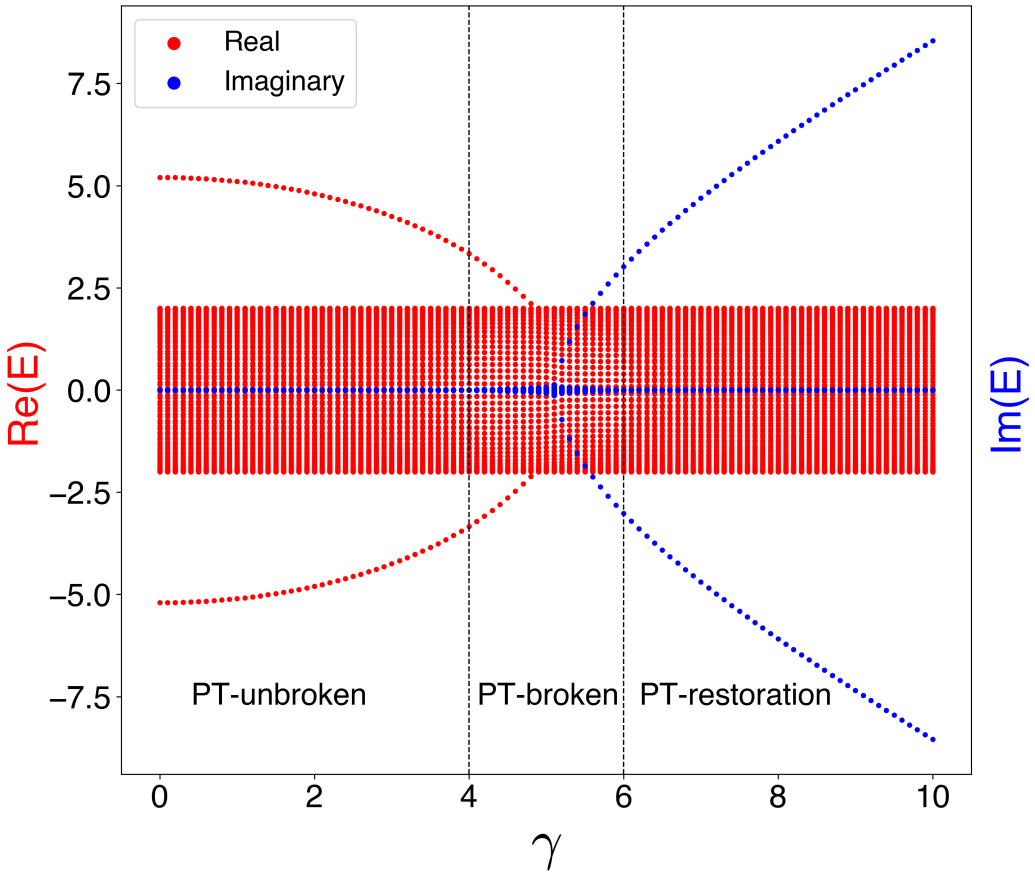

Figure 5.9: Energy spectrum of the disorder free case with respect to γ for a fixed $\delta = 5t$ value. Real parts of the eigenvalues are marked in red, imaginary parts of the eigenvalues are marked in blue.

Chapter 6

Size-Dependent Anderson Localization

In this chapter, we introduce random on-site potentials into the 1D lattice with non-reciprocal impurity to observe size-dependent Anderson localization. This forms the main result of the thesis.

6.1 Extended Model

Consider a one-dimensional disordered Hermitian lattice with a non-Hermitian impurity, as illustrated in Fig. 6.1. The Hamiltonian is given by

$$\begin{aligned}\hat{H} = &\sum_{n\neq m} t(\hat{c}_{n+1}^{\dagger}\hat{c}_n + \text{H.c.}) + \sum_{n=1}^{N} V_n \hat{c}_n^{\dagger}\hat{c}_n \\ &+ (\delta-\gamma)\hat{c}_{m+1}^{\dagger}\hat{c}_m + (\delta+\gamma)\hat{c}_m^{\dagger}\hat{c}_{m+1},\end{aligned} \tag{6.1}$$

where t is the hopping constant between neighbouring sites, $\hat{c}_n$ ($\hat{c}_n^{\dagger}$) annihilation(creation) operators at site n, δ and γ define the local non-Hermitian impurity at site m, V_n represents random uncorrelated on-site energies uniformly

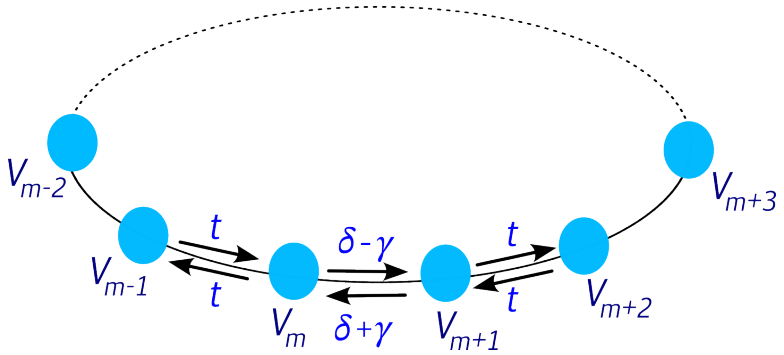

Figure 6.1: 1D Hermitian lattice with a non-Hermitian impurity. t's are the Hermitian hoppings between the neighboring sites, on-site potentials are V_m and non-Hermitian impurity at site m has $\delta - \gamma$ to the right and $\delta + \gamma$ to the left. The Hermitian Anderson model shows an Anderson transition at any non-zero disorder strength. Adding a single impurity makes the Anderson transition point dependent on the system size. In the Hermitian Anderson model, extended states become Anderson localized states at the Anderson transition point. However, when a single impurity is introduced, both extended and SFL states turn into Anderson localized states at the transition point. This leads to a significant shift and size dependency in the Anderson transition point.

distributed in the interval of $W[-0.5, 0.5]$ with W being the disorder strength and $\gamma, \delta, W \in \mathbb{R}$. For PBC, assume that $\hat{c}_{N+1} = \hat{c}_1$. We will set $t = 1$ for simplicity when performing numerical calculations.

We can rewrite Eq.6.1 for PBC without using second quantized operators and in bra-ket notation

$$\begin{aligned}\hat{H}_{\text{PBC}} = &\sum_{n=1}^{N-1} t(|n\rangle\langle n+1| + |n+1\rangle\langle n|) + t(|N\rangle\langle 1| + |1\rangle\langle N|) \\ &+ (\delta-\gamma)|m+1\rangle\langle m| + (\delta+\gamma)|m\rangle\langle m+1| \\ &+ \sum_{n=1}^{N} V_n |n\rangle\langle n|\end{aligned} \tag{6.2}$$

Its matrix representation of the model is as follows

$$\begin{pmatrix} V_1 & t & 0 & \cdots & 0 & 0 & \cdots & 0 & t \\ t & V_2 & t & \cdots & 0 & 0 & \cdots & 0 & 0 \\ 0 & t & V_3 & \ddots & \vdots & \vdots & & \vdots & \vdots \\ \vdots & \vdots & \vdots & \ddots & V_m & \delta+\gamma & \cdots & & \vdots \\ \vdots & \vdots & \vdots & & \delta-\gamma & V_{m+1} & \cdots & & \vdots \\ \vdots & \vdots & \vdots & & \vdots & & \ddots & \vdots & \vdots \\ 0 & 0 & 0 & \cdots & 0 & 0 & \cdots & V_{N-1} & t \\ t & 0 & 0 & \cdots & 0 & 0 & \cdots & t & V_N \end{pmatrix}_{N\times N}, \tag{6.3}$$

where non-Hermitian impurity couplings are highlighted in blue: $\delta-\gamma$ and $\delta+\gamma$; PBC is assured with the red highlighted t's. This matrix will be used to find eigenvalues and eigenvectors in numerical calculations of a one-dimensional disordered Hermitian lattice with a non-Hermitian impurity.

The eigenvalue equation is given by $\hat{H}\left|\psi\right\rangle = E\left|\psi\right\rangle$, where $\left|\psi\right\rangle$ can be written as a linear combination of the basis states as

$$\left|\psi\right\rangle = \sum_n \psi_n \hat{c}_n^\dagger \left|0\right\rangle, \tag{6.4}$$

where ψ_n describes the probability amplitude of the eigenstate at site n. We can write eigenvalue equation for $n \neq m, m+1$ as

$$t\psi_{n+1} + t\psi_{n-1} + V_n\psi_n = E\psi_n, \tag{6.5}$$

and eigenvalue equations for the impurity sites are

$$\begin{aligned} t\psi_{m-1} + (\delta+\gamma)\psi_{m+1} + V_m\psi_m &= E\psi_m, \\ t\psi_{m+2} + (\delta-\gamma)\psi_m + V_{m+1}\psi_{m+1} &= E\psi_{m+1}. \end{aligned} \tag{6.6}$$

6.2 Results

6.2.1 General Traits

Since we introduce disorder to the model in this section, we first want to observe what changes occur in the disorder-free complex count shown in Fig. 5.2 when disorder is introduced. Results are shown in Fig. 6.2. The number of complex eigenvalues are plotted as a function of δ and γ for $N = 40$ and different disorder strengths. In both the PT-unbroken and PT-restoration regions, the introduction of disorder does not alter the eigenvalues' behavior as they remain real in the absence of disorder, except for the two-impurity bound states, which exhibit complex eigenvalues in the PT-restoration region. Excluding the two-impurity bound states in the PT-restoration region, the eigenvalues remain real. In the PT-broken region, when disorder is introduced to the system, the energy spectrum under PBC begins to transition from forming a loop in the complex plane to coalescing onto the real axis. As the disorder increases, the number of complex eigenvalues decreases. If the disorder strength is sufficiently strong, the entire energy spectrum of the system will lie on the real axis.

In Chapter 4, we discussed about how to find the critical disorder strength W_c at which Anderson transition occurs. Now, we will find the W_c for the impurity induced disordered 1D lattice for various different lattice sizes and compare them. At the critical disorder strength, all eigenstates have real eigenvalues as we discussed in the previous chapters.

For the disorder-free case, we showed in Chapter 5 that there are two impurity-bound states in each PT-unbroken, PT-broken and PT-restoration regions. Excluding the energies of these two impurity-bound states, W_c is the point where the both the PBC and OBC spectrum coalesce to the real axis.

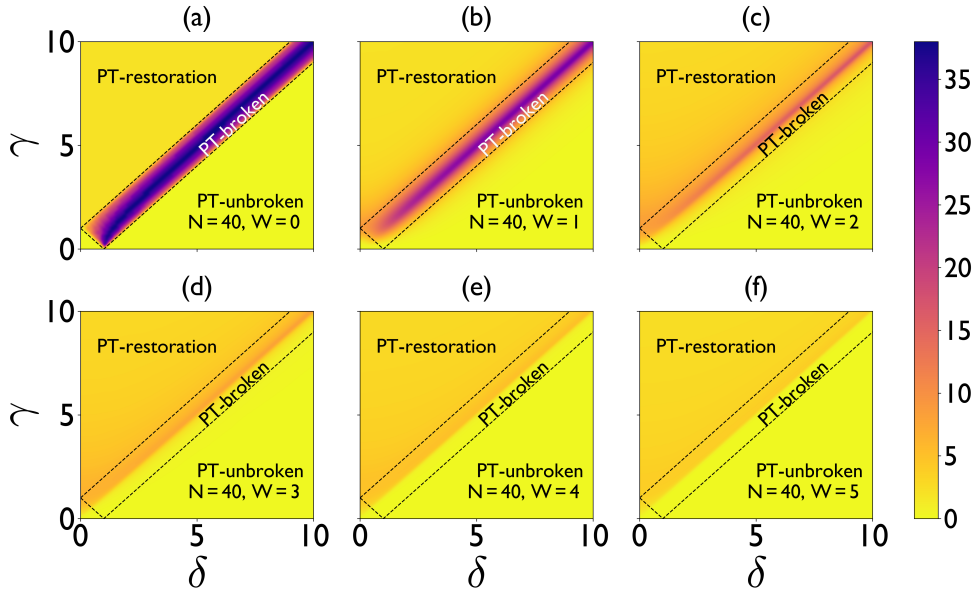

Figure 6.2: Phase diagram of the 1D lattice in Eq.6.1 for different W, disorder strength values. The number of complex eigenvalues are coded in the color bar as a function of δ and γ for $N = 40$ and (a) $W = 0$, "Disorder-free" , (b) $W = 1$, (c) $W = 2$, (d) $W = 3$, (e) $W = 4$, (f) $W = 5$

6.2.2 Critical Disorder Strength

In Fig. 6.3, we numerically calculated the critical disorder strength W_c for lattice sizes $N = 40, 80, 160$ and 1000 and W_c is plotted as a function of δ and γ. This process is averaged over many random potential realizations since W_c changes with each choice of random potential sets. High sensitivity to the boundary conditions disappears at the critical disorder strength.

Fig. 6.3 will be analyzed in three distinct regions:

1. PT-unbroken,
2. PT-restoration,
3. PT-broken.

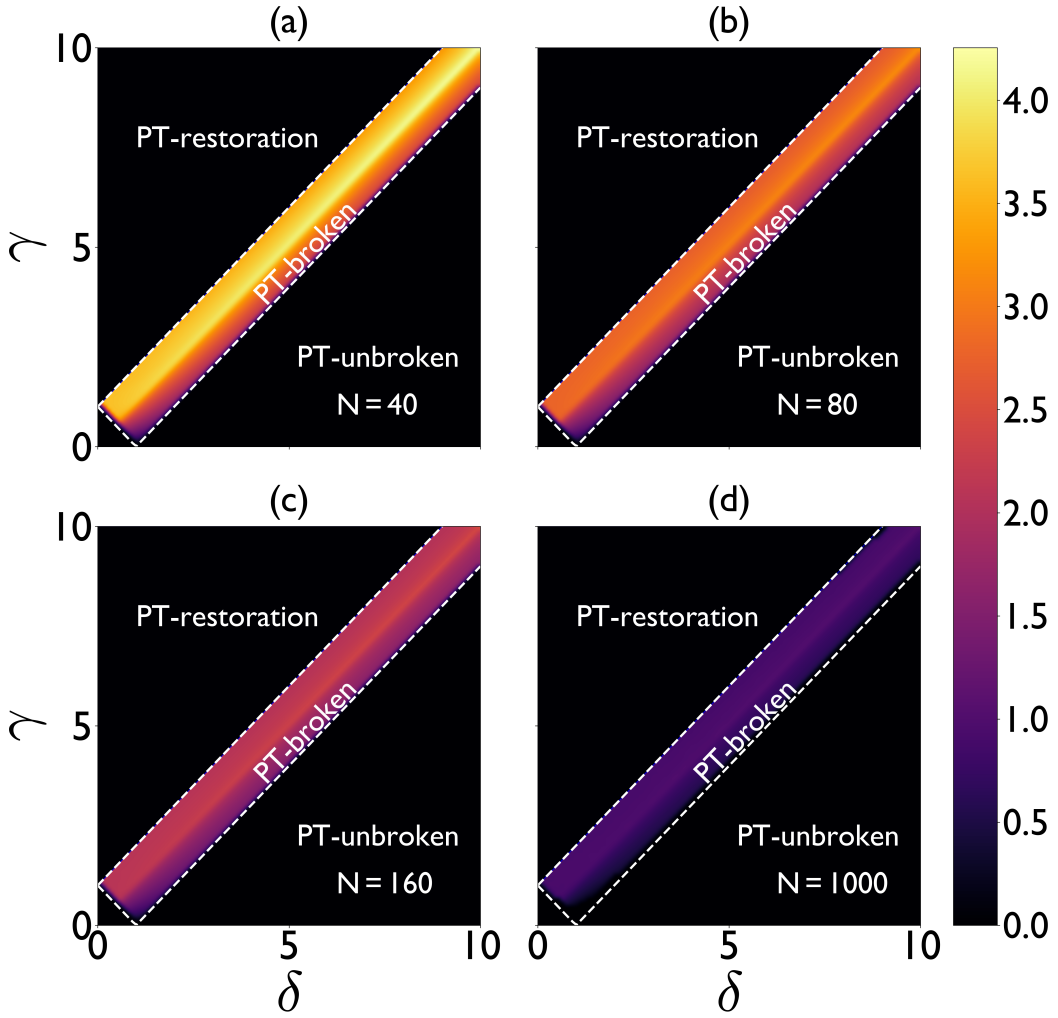

Figure 6.3: Phase diagram of the critical disorder strength (W_c) as a function of δ and γ for different system sizes: (a) $N = 40$, (b) $N = 80$, (c) $N = 160$, (d) $N = 1000$ for $t = 1$. White dashed lines are given by $\gamma = |\delta - t|$ and $\gamma = \delta + t$ and represent the phase boundaries of the PT-symmetry for there regions. PT-unbroken region where $\gamma < |\delta - t|$, PT-broken region where $|\delta - t| < \gamma < \delta + t$, PT-restoration region where $\gamma > \delta + t$. Results are averaged over many random potential realizations. Impurity is positioned at $m = N/2$. Competition between Anderson and SFL states. Anderson and SFL states coexist until $W = W_c$ in which Anderson transition occurs.

6.2.3 PT-unbroken and PT-restoration Regions

Both PBC and OBC spectrum have real eigenvalues and lie on the real axis in the complex energy plane even in the disorder-free case in PT-unbroken region. We analyzed this behaviour in Chapter 5. Localization of eigenstates occurs with infinitesimally small random potentials like the Hermitian model. Thus, Anderson localization takes place at introducing infinitesimally small random potentials.

Similarly, excluding the two impurity-bound states that have complex eigenvalues, PBC and OBC spectrum lie on the real axis even in the disorder-free case as discussed in Chapter 5. Here, W_c is the point where extended bulk states turns into Anderson localized states. Both PBC and OBC spectrum coalesce into the real axis excluding the two impurity-bound states. Infinitesimally small random potentials cause the localization of the eigenstates like in the PT-unbroken region.

6.2.4 PT-broken Region

In the PT-broken region, the energy spectrum is highly sensitive to the boundary conditions. Energy spectrum can be significantly altered when boundaries are introduced. In the absence of disorder, the energy spectrum under PBC forms a loop on the complex energy plane while the energy spectrum under OBC lies on the real axis. With extended and SFL states co-existing under PBC, variation in the energy spectrum between PBC and OBC indicates the characteristic properties of the corresponding eigenstates. When we introduce disorder into the system, extended and SFL states start to transform into localized ones. First, the extended state with the highest absolute value of the imaginary part of the energy becomes localized. Then, the SFL state with the smallest absolute value of the imaginary part becomes localized. Last one the localize is the SFL state with the highest imaginary part of the eigenvalue. Fig. 6.4 shows the ratio of the Anderson localized states over all states. Up to W_c, all states turn into Anderson localized states one by one, so the ratio is increasing. At W_c all states becomes Anderson localized states.

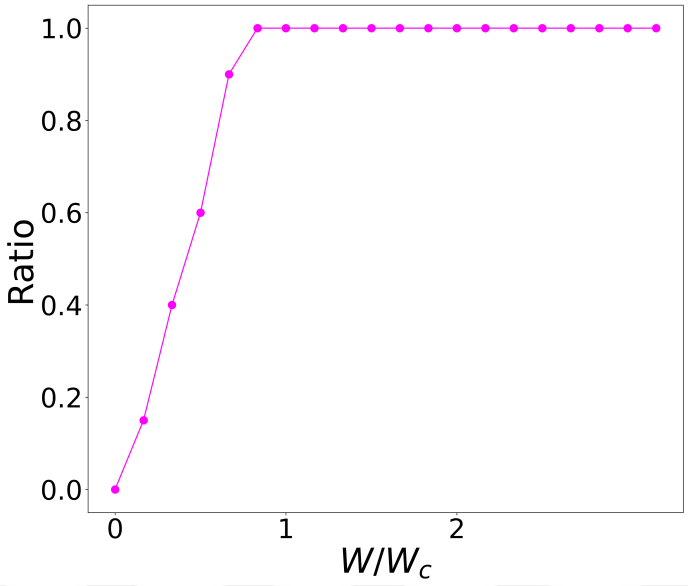

Figure 6.4: Ratio of the Anderson localized states over all states at $\gamma = \sqrt{\delta^2 - t^2}$.

For the PT-broken region, the critical disorder strength W_c is the point where extended and SFL states turn into Anderson localized ones. At this point, energy spectrum is no longer highly sensitive to the boundary conditions. Since SFL and extended states are the ones that become Anderson localized states, this contrasts with the Hatano-Nelson model that is discussed in Chapter 4 where skin states turn into Anderson localized states with the introduction of disorder and thus leading the formation of the mobility edge in one dimension. These mobility edges are the critical energy values that separate localized states from extended states. In other words, states below the mobility edge are typically Anderson localized, while states above it are extended [32, 33, 34, 35, 36, 37].

Note that skin states are characterized by their size-independent localization lengths, meaning that their localization lengths remain constant regardless of the system size. As a result, the Anderson localization transition point in the Hatano-Nelson model does not depend on the system size. Our results in Chapter 4 demonstrate the size independency of W_c in Hatano-Nelson model. In this chapter, the model is also different from the Hermitian Anderson model, where

mobility edge is absent. This is because all disorder-free states are extended, which localize in the presence of disorder. When a single impurity is introduced into the Hermitian Anderson model, not only extended but also SFL states turn into Anderson localized states, leading to size-dependent transition point due to the size-dependent character of the SFL states. This shows how an impurity changes the Anderson transition point, which has no Hermitian counterpart. Note that the fraction of extended states to SFL states varies with the parameters δ and γ. Therefore, the Anderson transition point changes with these parameters.

At $\gamma = \sqrt{\delta^2 - 1}$, all disorder-free states become SFL states [71]. We perform numerical analysis to obtain W_c as a function of δ and γ, and present our results in Fig. 6.3. As shown, there is a sharp transition in W_c at the boundary between the PT-broken and other regions. In the PT-broken region with a fixed δ, W_c increases until it reaches its maximum value at $\gamma = \sqrt{\delta^2 - 1}$, then decreases until it reaches the border between the PT-broken and PT-restoration regions. The size-dependency of the Anderson transition point is evident from the figure. As illustrated in Fig. 6.3, increasing the lattice size from $N = 40$ to 1000 leads to a decrease in the critical disorder strength, W_c. For $N = 1000$, it is observed that in the PT-broken region, the maximum value of W_c is close to one, indicating that Anderson localization begins to appear even at a weak value of disorder. Note that W_c approaches zero in the thermodynamic limit.

6.2.5 IPR Values

Anderson localization might occur at arbitrary values of disorder strength in the PT-unbroken and the PT-restoration regions. In practical terms, a lattice has a finite and limited length. When W is greater than the critical disorder strength W_c, localization length may surpass the system size. As a result, the corresponding states act as they are delocalized and exhibit a delocalized behaviour. Likewise, localization lengths of the eigenstates may exceed the system size in PT-broken region. Thus, Anderson localization might not be observed.

Inverse participation ratio (IPR) is used to study the localization properties of

the eigenstates. As stated in Section 1.1.5, IPR is a measure of the localization of an eigenstate with energy E and defined as

$$\text{IPR} = \frac{\sum_n |\psi_n|^4}{\left(\sum_n |\psi_n|^2\right)^2}, \tag{6.7}$$

where ψ_n at energy represents the states at energy E.

IPR values range between 0 and 1. A more localized state, has a higher IPR value. IPR value of a completely localized state is 1. When a state is delocalized meaning that its amplitude spreads more evenly across many sites, IPR value is close to 0. For a completely delocalized state, IPR value approaches to $1/N$. The average IPR is calculated as the average of all individual IPR values at each energy level and this is averaged over many realizations. Intermediate IPR values indicate partial localization, with the amplitude distributed over several sites but not uniformly.

To observe the localization properties of the eigensates, the eigenstate with the lowest IPR value for each W is calculated and averaged over 10000 realizations and compared to that of the Hermitian Anderson model, as shown in Fig. 6.5. The eigenstate with the lowest IPR value is the one that is most delocalized and is the last to transition into the Anderson localized state. This particular state also corresponds to the SFL state with the highest imaginary value for the disorder-free case, $W = 0$.

As depicted in Fig. 6.5, the SFL state with the minimum IPR value first becomes more extended with increasing disorder, resulting in a decrease in the IPR value for all cases for $N = 40, 80$ and 160. Following the decrease in the IPR value, SFL states start to become more localized and thus have higher IPR values. In the Hermitian case, we observe a different and somewhat opposite behaviour. States with the lowest IPR value initially becomes more localized and have higher IPR values monotonically with increasing disorder. Fig. 6.5 shows that non-Hermitian and Hermitian systems start to overlap near the critical

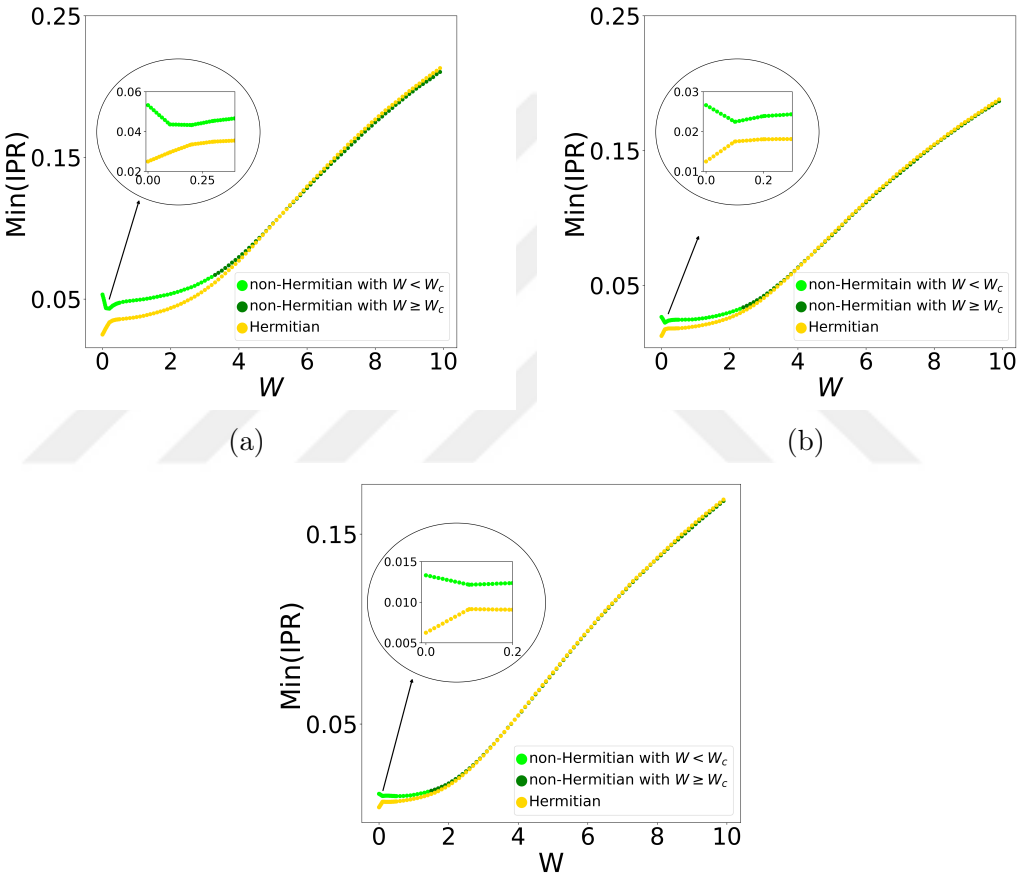

(a) (b) (c)

Figure 6.5: The minimum IPR among all IPR values as a function of disorder strength, averaged over 10000 realizations for both Hermitian (yellow) and non-Hermitian (lime for $W < W_c$ and green for $W \geq W_c$) cases when $\gamma = \sqrt{\delta^2 - t^2}$ for (a) $N = 40$, (b) $N = 80$ (c) $N = 160$.

disorder strength, W_c. This overlap approaches to W_c with higher lattice sizes as it can be seen in Fig. 6.5a, 6.5b and 6.5c.

We can also observe the size dependency of the critical disorder strength in Fig. 6.5a, Fig. 6.5b and Fig. 6.5c. After the Anderson transition at W_c, all states are Anderson localized and min(IPR) values start to increase with a increasing disorder. The number and strength of Anderson localized states increase with a increasing disorder strength while the mobility and SFL modes shrink towards the real axis. Fig. 6.5 also shows a size-dependent localization by observing the critical disorder strength points of different lattice sizes, $N = 40, 80$ and 160. When $N = 160$, we can see that non-Hermitian and Hermitian case overlaps before $N = 40$ and $N = 80$, meaning that $N = 160$ has a lower critical disorder point. Same applies for $N = 40$ and $N = 80$. W_c is decreasing with higher lattice sizes as the overlap point of the Hermitian and non-Hermitian case happens at lower W values.

Next, *average* IPR values of all states at the critical disorder strength is observed. Fig. 6.6 shows the average IPR of all individual IPR values at the Anderson transition point, $(W = W_c)$, for the lattice sizes $N = 40, 80, 160$ and 1000. This procedure is averaged over many realizations. At the critical disorder strength, W_c, the average IPR values are moderate, suggesting that a large portion of eigenstates are localized with smaller localization lengths than the system size, while a few are acting as if they are delocalized as their localization lengths exceed the system size. Fig. 6.6 also shows a decrease in average IPR values with higher lattice sizes which can be observed in the color codes. Average IPR values approach zero in thermodynamic limit. This indicates that the size dependency is more significant for smaller lattice sizes. It is noteworthy that Anderson localized states in PT-broken region have shorter localization lengths than the Anderson localized states of PT-unbroken and PT-restoration regions. Since, in the PT-broken region SFL states turns into Anderson localized states and localization length of SFL states scales with system size unlike the skin states. Consequently, the average IPR values undergo a sharp transition for the same disorder strength at the boundaries between PT-broken and other regions.

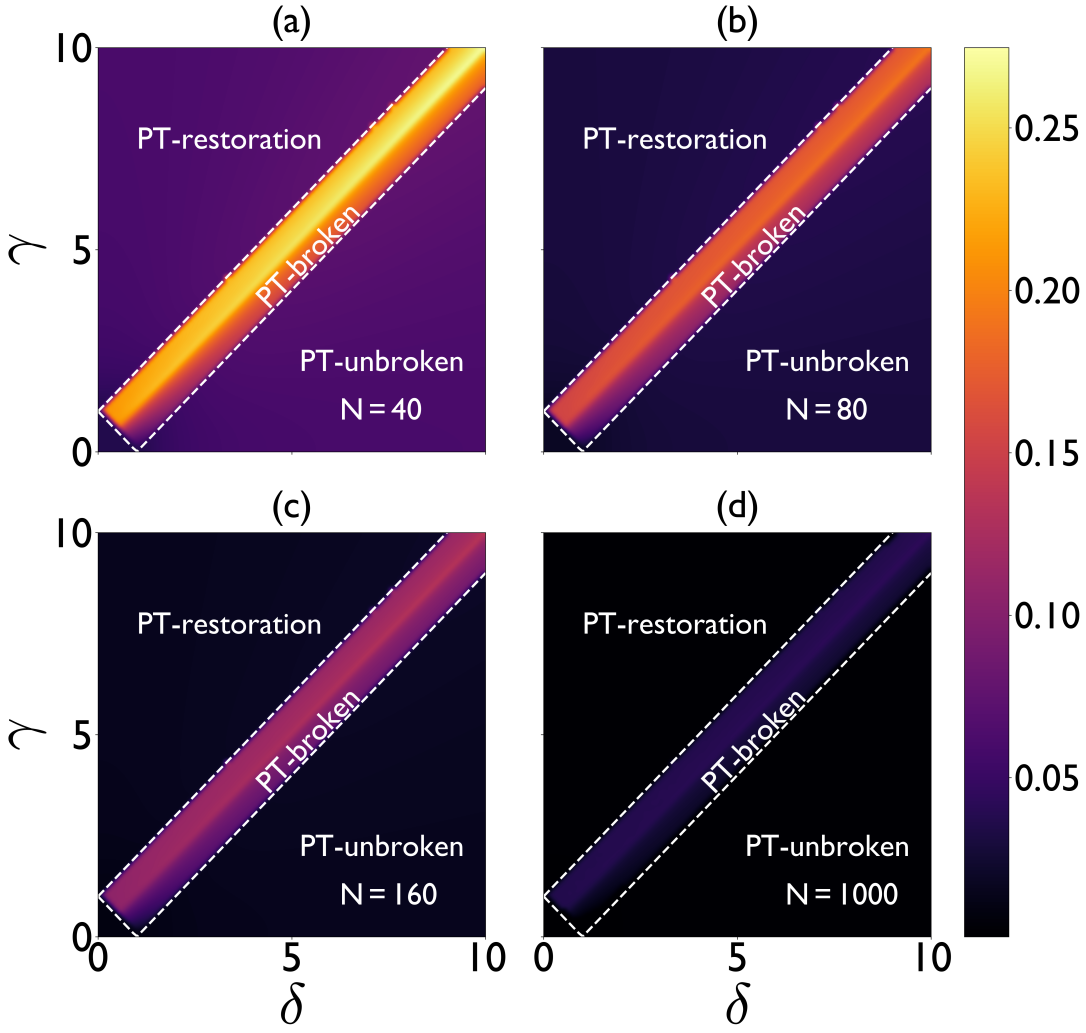

Figure 6.6: Average IPR values at $W = W_c$ for various system sizes: (a) $N = 40$, (b) $N = 80$, (c) $N = 160$, and (d) $N = 1000$. The white dashed lines are given by $\gamma = |\delta - t|$ and $\gamma = \delta + t$. Notice the difference in average IPR values between the PT-broken region and the other two regions at the same disorder strength. This difference arises because SFL states transform into Anderson localized states in the PT-broken region, whereas extended states undergo this transformation in the other regions. Impurity is positioned at $m = N/2$.

Chapter 7

Conclusion

To summarize, we have studied the localization properties of the 1D Hatano-Nelson model with and without disorder, and 1D Hermitian lattice with a non-Hermitian impurity.

We stated that for a Hermitian Anderson model, Anderson transition occurs at infinitesimally small disorder strength and is not size-dependent. Then, 1D Hatano-Nelson model exhibiting NHSE is studied. Bulk-boundary correspondence in Hermitian systems gets a modification in non-Hermitian systems and is related to the emergence of NHSE. With introducing disorder to the Hatano-Nelson model, we can observe the competition between NHSE and Anderson localization. The critical disorder strength W_c is the point where the Anderson transition takes place. Since the localization length of the skin states are not dependent on the lattice size, a size-independent Anderson localization occurs.

Restoring the lattice to be Hermitian but introducing a non-reciprocally-coupled impurity gives rise to a unique localization called SFL. The spatial decay length of SFL states is not fixed and scales with the size of the system while the profile of SFL states is not dependent on the size, thus the name scale-free. We observe the competition between SFL and Anderson localized states. Since the localization length of SFL states scales with the system size a size-dependent

Anderson localization emerges. When the lattice size is increased, there is a corresponding decrease in the W_c value.

For future work, complex on-site energies, complex hopping terms or complex impurity can be introduced into the different lattice models and higher-dimensional systems to observe the behaviour of non-Hermitian skin effect and scale-free localization. In addition, in this thesis we worked with a specific 1D lattice model to show size-dependent Anderson localization. Working with higher dimensions and different lattice models can forge the versatility of size-dependent Anderson localization. In addition, by introducing a non-reciprocal impurity to Hofstadter's butterfly model, the model can be made non-Hermitian and the eigenvalues and eigenstates can be investigated.

Bibliography

[1] C. M. Bender, *PT symmetry in quantum and classical physics*. World Scientific, 2018.

[2] C. M. Bender and S. Boettcher, "Real spectra in non-hermitian hamiltonians having PT symmetry," *Phys. Rev. Lett.*, vol. 80, pp. 5243–5246, Jun 1998.

[3] C. M. Bender, S. Boettcher, and P. N. Meisinger, "PT-symmetric quantum mechanics," *Journal of Mathematical Physics*, vol. 40, pp. 2201–2229, 05 1999.

[4] R. El-Ganainy, K. G. Makris, M. Khajavikhan, Z. H. Musslimani, S. Rotter, and D. N. Christodoulides, "Non-hermitian physics and pt symmetry," *Nature Physics*, vol. 14, p. 11–19, Jan 2018.

[5] V. V. Konotop, J. Yang, and D. A. Zezyulin, "Nonlinear waves in $\mathcal{PT}$-symmetric systems," *Rev. Mod. Phys.*, vol. 88, p. 035002, Jul 2016.

[6] Z. G. Yuto Ashida and M. Ueda, "Non-hermitian physics," *Advances in Physics*, vol. 69, no. 3, pp. 249–435, 2020.

[7] M.-H. L. Xiujuan Zhang, Tian Zhang and Y.-F. Chen, "A review on non-hermitian skin effect," *Advances in Physics: X*, vol. 7, no. 1, p. 2109431, 2022.

[8] C.-X. Guo, X. Wang, H. Hu, and S. Chen, "Accumulation of scale-free localized states induced by local non-hermiticity," *Phys. Rev. B*, vol. 107, p. 134121, Apr 2023.

[9] P. Wang, L. Jin, and Z. Song, "Non-hermitian phase transition and eigenstate localization induced by asymmetric coupling," *Phys. Rev. A*, vol. 99, p. 062112, Jun 2019.

[10] K.-M. Kim and M. J. Park, "Disorder-driven phase transition in the second-order non-hermitian skin effect," *Phys. Rev. B*, vol. 104, p. L121101, Sep 2021.

[11] S. Ghosh, S. Gupta, and M. Kulkarni, "Spectral properties of disordered interacting non-hermitian systems," *Phys. Rev. B*, vol. 106, p. 134202, Oct 2022.

[12] Z.-Q. Zhang, H. Liu, H. Liu, H. Jiang, and X. Xie, "Bulk-boundary correspondence in disordered non-hermitian systems," *Science Bulletin*, vol. 68, no. 2, pp. 157–164, 2023.

[13] G. De Tomasi and I. M. Khaymovich, "Non-hermiticity induces localization: Good and bad resonances in power-law random banded matrices," *Phys. Rev. B*, vol. 108, p. L180202, Nov 2023.

[14] D. Kochergin, V. Tiselko, and A. Onuchin, "Localization transition in non-hermitian systems depending on reciprocity and hopping asymmetry," *Phys. Rev. E*, vol. 109, p. 044315, Apr 2024.

[15] J.-W. Ryu, N. Myoung, A. Go, S. Woo, S.-J. Choi, and H. C. Park, "Emergent localized states at the interface of a twofold $\mathcal{PT}$-symmetric lattice," *Phys. Rev. Res.*, vol. 2, p. 033149, Jul 2020.

[16] L.-Z. Tang, L.-F. Zhang, G.-Q. Zhang, and D.-W. Zhang, "Topological anderson insulators in two-dimensional non-hermitian disordered systems," *Phys. Rev. A*, vol. 101, p. 063612, Jun 2020.

[17] L.-Z. Tang, G.-Q. Zhang, L.-F. Zhang, and D.-W. Zhang, "Localization and topological transitions in non-hermitian quasiperiodic lattices," *Phys. Rev. A*, vol. 103, p. 033325, Mar 2021.

[18] L.-Z. Tang, S.-N. Liu, G.-Q. Zhang, and D.-W. Zhang, "Topological anderson insulators with different bulk states in quasiperiodic chains," *Phys. Rev. A*, vol. 105, p. 063327, Jun 2022.

[19] A. P. Acharya, A. Chakrabarty, D. K. Sahu, and S. Datta, "Localization, $\mathcal{PT}$ symmetry breaking, and topological transitions in non-hermitian quasicrystals," *Phys. Rev. B*, vol. 105, p. 014202, Jan 2022.

[20] A. Padhan, S. R. Padhi, and T. Mishra, "Complete delocalization and reentrant topological transition in a non-hermitian quasiperiodic lattice," *Phys. Rev. B*, vol. 109, p. L020203, Jan 2024.

[21] S. Yao and Z. Wang, "Edge states and topological invariants of non-hermitian systems," *Phys. Rev. Lett.*, vol. 121, p. 086803, Aug 2018.

[22] H. Jiang, L.-J. Lang, C. Yang, S.-L. Zhu, and S. Chen, "Interplay of non-hermitian skin effects and anderson localization in nonreciprocal quasiperiodic lattices," *Phys. Rev. B*, vol. 100, p. 054301, Aug 2019.

[23] L. Li, C. H. Lee, S. Mu, and J. Gong, "Critical non-hermitian skin effect," *Nat. Commun.*, vol. 11, p. 5491, 2020.

[24] K. Yokomizo and S. Murakami, "Scaling rule for the critical non-hermitian skin effect," *Phys. Rev. B*, vol. 104, p. 165117, Oct 2021.

[25] C. E. Rüter, K. G. Makris, R. El-Ganainy, D. N. Christodoulides, M. Segev, and D. Kip, "Observation of parity-time symmetry in optics," *Nature Physics*, vol. 6, p. 192, 2010.

[26] B. Peng, K. Özdemir, F. Lei, F. Monifi, M. Gianfreda, G. L. Long, S. Fan, F. Nori, C. M. Bender, and L. Yang, "Parity-time-symmetric whispering-gallery microcavities," *Nature Physics*, vol. 10, p. 394, 2014.

[27] L. Feng, Z. J. Wong, R.-M. Ma, Y. Wang, and X. Zhang, "Single-mode laser by parity-time symmetry breaking," *Science*, vol. 346, p. 972, 2014.

[28] L. Xiao, X. Zhan, Z. H. Bian, K. K. Wang, X. Zhang, X. P. Wang, J. Li, K. Mochizuki, D. Kim, N. Kawakami, W. Yi, H. Obuse, B. C. Sanders, and

P. Xue, "Observation of topological edge states in parity-time-symmetric quantum walks," *Nature Physics*, vol. 13, p. 1117, 2017.

[29] S. Weimann, M. Kremer, Y. Plotnik, Y. Lumer, S. Nolte, K. G. Makris, M. Segev, M. C. Rechtsman, and A. Szameit, "Topologically protected bound states in photonic parity-time-symmetric crystals," *Nature Materials*, vol. 16, p. 433, 2017.

[30] W. D. Heiss, "The physics of exceptional points," *Journal of Physics A: Mathematical and Theoretical*, vol. 45, p. 444016, 2012.

[31] P. W. Anderson, "Absence of diffusion in certain random lattices," *Phys. Rev.*, vol. 109, pp. 1492–1505, Mar 1958.

[32] Z. Gong, Y. Ashida, K. Kawabata, K. Takasan, S. Higashikawa, and M. Ueda, "Topological phases of non-hermitian systems," *Phys. Rev. X*, vol. 8, p. 031079, Sep 2018.

[33] Q.-B. Zeng and Y. Xu, "Winding numbers and generalized mobility edges in non-hermitian systems," *Phys. Rev. Res.*, vol. 2, p. 033052, Jul 2020.

[34] Y. Liu, Y. Wang, X.-J. Liu, Q. Zhou, and S. Chen, "Exact mobility edges, pt-symmetry breaking, and skin effect in one-dimensional non-hermitian quasicrystals," *Phys. Rev. B*, vol. 103, p. 014203, 2021.

[35] S. Mu, L. Zhou, L. Li, and J. Gong, "Non-hermitian pseudo mobility edge in a coupled chain system," *Phys. Rev. B*, vol. 105, p. 205402, May 2022.

[36] W. Han and L. Zhou, "Dimerization-induced mobility edges and multiple reentrant localization transitions in non-hermitian quasicrystals," *Phys. Rev. B*, vol. 105, p. 054204, Feb 2022.

[37] Q. Tang and Y. He, "Mobility edges in non-hermitian models with slowly varying quasiperiodic disorder," *Phys. Rev. B*, vol. 109, p. 224204, Jun 2024.

[38] C. Yuce and H. Ramezani, "Coexistence of extended and localized states in the one-dimensional non-hermitian anderson model," *Phys. Rev. B*, vol. 106, p. 024202, Jul 2022.

[39] N. Okuma and M. Sato, "Non-hermitian topological phenomena: A review," *Annual Review of Condensed Matter Physics*, vol. 14, p. 83–107, Mar 2023.

[40] N. Okuma, K. Kawabata, K. Shiozaki, and M. Sato, "Topological origin of non-hermitian skin effects," *Phys. Rev. Lett.*, vol. 124, p. 086801, Feb 2020.

[41] C. Yuce, "Nonlinear non-hermitian skin effect," *Physics Letters A*, vol. 408, p. 127484, 2021.

[42] J. Claes and T. L. Hughes, "Skin effect and winding number in disordered non-hermitian systems," *Phys. Rev. B*, vol. 103, p. L140201, Apr 2021.

[43] S. M. Rafi-Ul-Islam, Z. B. Siu, H. Sahin, C. H. Lee, and M. B. A. Jalil, "Critical hybridization of skin modes in coupled non-hermitian chains," *Phys. Rev. Research*, vol. 4, p. 013243, 2022.

[44] Z. Ozcakmakli Turker and C. Yuce, "Open and closed boundaries in non-hermitian topological systems," *Phys. Rev. A*, vol. 99, p. 022127, Feb 2019.

[45] Z. Yang, K. Zhang, C. Fang, and J. Hu, "Non-hermitian bulk-boundary correspondence and auxiliary generalized brillouin zone theory," *Phys. Rev. Lett.*, vol. 125, p. 226402, Nov 2020.

[46] Y. Yi and Z. Yang, "Non-hermitian skin modes induced by on-site dissipations and chiral tunneling effect," *Phys. Rev. Lett.*, vol. 125, p. 186802, 2020.

[47] B. Many Manda, R. Carretero-González, P. G. Kevrekidis, and V. Achilleos, "Skin modes in a nonlinear hatano-nelson model," *Phys. Rev. B*, vol. 109, p. 094308, Mar 2024.

[48] K. Xu, X. Zhang, K. Luo, R. Yu, D. Li, and H. Zhang, "Coexistence of topological edge states and skin effects in the non-hermitian su-schrieffer-heeger model with long-range nonreciprocal hopping in topoelectric realizations," *Phys. Rev. B*, vol. 103, p. 125411, Mar 2021.

[49] T. Helbig, T. Hofmann, S. Imhof, M. Abdelghany, T. Kiessling, L. W. Molenkamp, C. H. Lee, A. Szameit, M. Greiter, and R. Thomale, "Generalized bulk–boundary correspondence in non-hermitian topolectrical circuits," *Nature Physics*, vol. 16, p. 747–750, Jun 2020.

[50] S. Liu, R. Shao, S. Ma, L. Zhang, O. You, H. Wu, Y. J. Xiang, T. J. Cui, and S. Zhang, "Non-hermitian skin effect in a non-hermitian electrical circuit," *Research*, vol. 2021, 2021.

[51] B. Li, H.-R. Wang, F. Song, and Z. Wang, "Scale-free localization and $\mathcal{PT}$ symmetry breaking from local non-hermiticity," *Phys. Rev. B*, vol. 108, p. L161409, Oct 2023.

[52] P. Molignini, O. Arandes, and E. J. Bergholtz, "Anomalous skin effects in disordered systems with a single non-hermitian impurity," *Phys. Rev. Research*, vol. 5, p. 033058, 2023.

[53] W. Li, Z. Sun, Z. Yang, and F. Li, "Universal scalefree non-hermitian skin effect near the bloch point," *Phys. Rev. B*, vol. 109, p. 035119, 2024.

[54] B. Li, H.-R. Wang, F. Song, and Z. Wang, "Scale-free localization and $\mathcal{PT}$ symmetry breaking from local non-hermiticity," *Phys. Rev. B*, vol. 108, p. L161409, Oct 2023.

[55] X. Xie, G. Liang, F. Ma, Y. Du, Y. Peng, E. Li, H. Chen, L. Li, F. Gao, and H. Xue, "Observation of scale-free localized states induced by non-hermitian defects," *Phys. Rev. B*, vol. 109, p. L140102, Apr 2024.

[56] S. A. Trugman, "Localization, percolation, and the quantum hall effect," *Phys. Rev. B*, vol. 27, pp. 7539–7546, Jun 1983.

[57] L. Li, C. H. Lee, and J. Gong, "Impurity induced scale-free localization," *Communications Physics*, vol. 4, p. 42, 2021.

[58] S. Hikami, "Localization Length and Inverse Participation Ratio of Two Dimensional Electron in the Quantized Hall Effect," *Progress of Theoretical Physics*, vol. 76, pp. 1210–1221, 12 1986.

[59] C. Kittel, P. McEuen, and J. W. . Sons, *Introduction to Solid State Physics*. John Wiley & Sons, 2005.

[60] K. Yokomizo and S. Murakami, "Non-bloch band theory of non-hermitian systems," *Phys. Rev. Lett.*, vol. 123, p. 066404, Aug 2019.

[61] M. Z. Hasan and C. L. Kane, "Colloquium: Topological insulators," *Rev. Mod. Phys.*, vol. 82, pp. 3045–3067, Nov 2010.

[62] D. Nakamura, T. Bessho, and M. Sato, "Bulk-boundary correspondence in point-gap topological phases," *Phys. Rev. Lett.*, vol. 132, p. 136401, Mar 2024.

[63] E. J. Bergholtz, J. C. Budich, and F. K. Kunst, "Exceptional topology of non-hermitian systems," *Rev. Mod. Phys.*, vol. 93, p. 015005, Feb 2021.

[64] L. Xiao, T. Deng, K. Wang, G. Zhu, Z. Wang, W. Yi, and P. Xue, "Non-hermitian bulk–boundary correspondence in quantum dynamics," *Nature Physics*, vol. 16, p. 761–766, Mar 2020.

[65] N. Hatano and D. R. Nelson, "Localization transitions in non-hermitian quantum mechanics," *Phys. Rev. Lett.*, vol. 77, pp. 570–573, Jul 1996.

[66] N. Hatano and D. R. Nelson, "Vortex pinning and non-hermitian quantum mechanics," *Phys. Rev. B*, vol. 56, pp. 8651–8673, Oct 1997.

[67] N. Hatano, "Localization in non-hermitian quantum mechanics and flux-line pinning in superconductors," *Physica A: Statistical Mechanics and its Applications*, vol. 254, no. 1, pp. 317–331, 1998.

[68] K. Yokomizo, T. Yoda, and S. Murakami, "Non-hermitian waves in a continuous periodic model and application to photonic crystals," *Phys. Rev. Res.*, vol. 4, p. 023089, May 2022.

[69] C.-X. Guo, C.-H. Liu, X.-M. Zhao, Y. Liu, and S. Chen, "Exact solution of non-hermitian systems with generalized boundary conditions: Size-dependent boundary effect and fragility of the skin effect," *Phys. Rev. Lett.*, vol. 127, p. 116801, Sep 2021.

[70] Q. Lin, T. Li, L. Xiao, K. Wang, W. Yi, and P. Xue, "Observation of non-hermitian topological anderson insulator in quantum dynamics," *Nature Communications*, vol. 13, p. 3229, Jun 2022.

[71] C.-X. Guo, X. Wang, H. Hu, and S. Chen, "Accumulation of scale-free localized states induced by local non-hermiticity," *Phys. Rev. B*, vol. 107, p. 134121, Apr 2023.